

Topological nature of edge states for one-dimensional systems without symmetry protection

Janet Zhong^{†,1}, Heming Wang^{†,2}, Alexander N. Poddubny,³ and Shanhui Fan^{1,2,*}

¹*Department of Applied Physics, Stanford University, Stanford, California 94305, USA*

²*Department of Electrical Engineering, Ginzton Laboratory, Stanford University, Stanford, California 94305, USA*

³*Department of Physics of Complex Systems, Weizmann Institute of Science, Rehovot 7610001, Israel*

[†]*These authors contributed equally to this work.*

(Dated: December 17, 2024)

We numerically verify and analytically prove a winding number invariant that correctly predicts the number of edge states in one-dimensional, nearest-neighbour (between unit cells), two-band models with any complex couplings and open boundaries. Our winding number uses analytical continuation of the wave-vector into the complex plane and involves two special points on the full Riemann surface band structure that correspond to bulk eigenvector degeneracies. Our invariant is invariant under unitary and similarity transforms. We emphasize that the topological criteria we propose here differ from what is traditionally defined as a topological or trivial phase in symmetry-protected classification studies. It is a broader invariant for our toy model that applies to non-zero energy edge states and its transition does not coincide with the gap closing condition. When the relevant symmetries are applied, our invariant reduces to well-known Hermitian and non-Hermitian symmetry-protected topological invariants.

Introduction– There has been substantial interest in the topology of band structures [1–3]. In Hermitian systems, the bulk-edge correspondence indicates the connection between topological invariants defined using the bulk states and the existence of zero-energy edge states [2, 4]. In one dimension, however, this correspondence is established only for systems with certain symmetries as classified under the ten Altland-Zirnbauer symmetry classes, known as the 10-fold way [2, 5–7]. In non-Hermitian systems, topological invariants for zero-energy edge states have also been established [8–15]. The required symmetry are classified by the 38-fold way [16, 17].

For one-dimensional Hermitian and non-Hermitian systems with no symmetry (class A), there has been no known topological invariant that corresponds to the existence of an edge state [6, 7, 16, 17]. In this paper, we will refer to class A models as symmetry-broken models. Although symmetry-broken models have no known topological invariants, they may still support edge states [18]. And moreover, the existence of these edge states may in general be quite robust. Introducing a symmetry-breaking perturbation to a model with symmetry eliminates the quantization of symmetry-protected topological invariants but the edge state itself usually persists [19–21]. Thus, edge states are more robust to perturbations as compared with the usual topological invariants [18, 22–26]. The observations above hint at the existence of a more general topological invariant that accounts for the robustness of the edge states without assuming the symmetry of the systems [19, 20, 27–37].

In this Letter, we consider a class of two-band models with complex couplings between nearest-neighbour unit

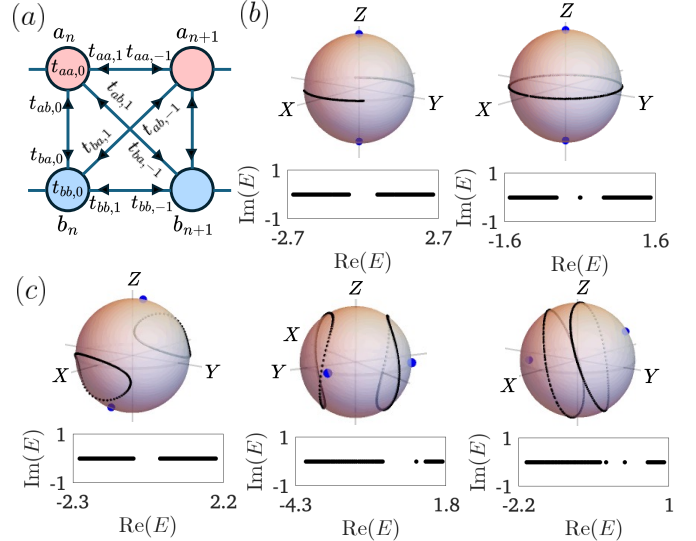


FIG. 1. (a) Two unit cells of the model in Eq. (1). (b) Hermitian SSH edge-state invariant on M -Riemann sphere (c) Hermitian random model and invariant on M -Riemann sphere corresponding to 0, 1 and 2 edge states. Model parameters are in SM Sec. I. Here, the two M_{deg} points are blue dots and the black loops are the image of the Brillouin zone on the M -Riemann sphere.

cells. This class of models have been extensively studied in the topological physics literature [2, 9, 11, 12, 19, 20, 27, 29, 31, 38–50]. We introduce a topological invariant for the existence of edge states in such models when an open boundary condition is imposed. This invariant builds entirely from properties of the bulk band structure and the bulk eigenstates, as described in the language of Riemann surfaces. It naturally reduces to known invariants in systems with symmetry and generalizes these

* shanhui@stanford.edu

known invariants to non-Hermitian systems without the need of symmetry constraints. The invariant takes a simplified form in Hermitian systems. Our results indicate the topological robustness of non-zero energy edge states for our model. We also show that the closure and emergence of edge states in symmetry-broken cases is not connected to the gap condition, and our invariant provides a measure of the strength of perturbation that is required in order to create or eliminate an edge state.

Model – We consider the following one-dimensional, two-band model as depicted in Fig. 1(a):

$$H(z) = \begin{pmatrix} t_{aa,0} + \frac{t_{aa,-1}}{z} + t_{aa,1}z & t_{ab,0} + \frac{t_{ab,-1}}{z} + t_{ab,1}z \\ t_{ba,0} + \frac{t_{ba,-1}}{z} + t_{ba,1}z & t_{bb,0} + \frac{t_{bb,-1}}{z} + t_{bb,1}z \end{pmatrix} \quad (1)$$

Here $z = e^{ik}$ is the phase factor, where k is the wave-vector and is in general complex [8]. This is the most general model containing only nearest neighbour coupling between unit cells. We are interested in the possible existence of edge states when the open boundary condition (OBC) of $\Psi_0 = \Psi_{N+1} = 0$ is imposed on the model. Here, Ψ_n is a vector representing the amplitudes at the sublattice sites within the n -th unit cell and N is the number of unit cells in a finite chain. For Hermitian models, we would have $t_{xy,n} = t_{yx,-n}^*$. Ref. [50] lists parameters within this model for all ten Hermitian symmetry classes. Eq. (1) can also be written as:

$$H(z) = \sum_{i=o,x,y,z} d_i(z)\sigma_i, \quad (2)$$

where σ_i are Pauli matrices and the d_i 's are in general complex for non-Hermitian systems. While $d_o(z)$ is sometimes omitted in previous studies, this term is quite important in non-Hermitian systems as its z dependence can change the eigenvalue braiding topology [51–56] (see Supplementary Material (SM) Sec. VIII [57] for more details).

The right eigenvalue equation of Eq. (1) reads

$$\begin{bmatrix} d_o(z) + d_z(z) & d_x(z) - id_y(z) \\ d_x(z) + id_y(z) & d_o(z) - d_z(z) \end{bmatrix} \begin{bmatrix} v_1^R \\ v_2^R \end{bmatrix} = E(z) \begin{bmatrix} v_1^R \\ v_2^R \end{bmatrix}, \quad (3)$$

where $E(z)$ is given by the characteristic polynomial

$$\det[H(z) - E(z)\mathbb{I}] = 0. \quad (4)$$

The study of topological edge states typically involves the integration of the Berry connection found from the bulk eigenvector of Eq. (1) over the Brillouin zone (BZ) for Hermitian cases [2, 58]). For non-Hermitian cases, we integrate over the generalized Brillouin zone (GBZ) [8, 9], as calculated from Eq. (4). For general cases of our model, Eq. (4) is a polynomial of degree two in E (as it is a two-band model) and a Laurent polynomial in z with exponents z^l where $-2 \leq l \leq 2$. There are four solutions for z at every E , and we number them in increasing order of magnitude $|z_1| \leq |z_2| \leq |z_3| \leq |z_4|$. Then the GBZ are the solutions in z for Eq. (4) when $|z_2| = |z_3|$. If

$-1 \leq l \leq 1$, we would use $|z_1| = |z_2|$ for the GBZ. For more details and more general cases of the GBZ, see Ref. [59].

We can study the eigenvector topology more easily by mapping the bulk eigenvector to $M \in \mathbb{C}$ where M is the ratio of the two bulk eigenvector elements $M(z) = v_1^R(z)/v_2^R(z)$ which can be found to be [60]:

$$M(z, E) = \frac{d_x(z) - id_y(z)}{E - d_o(z) - d_z(z)} = \frac{E - d_o(z) + d_z(z)}{d_x(z) + id_y(z)}. \quad (5)$$

For Hermitian systems with chiral or sublattice symmetry and where the model is in off-diagonal form, the typical topological invariant is the Berry-Zak phase [2, 58]:

$$W_{\text{BZ}}^{(i)} = \oint_{\mathcal{C}_{\text{BZ}}} \frac{1}{2\pi} \frac{d}{dz} \arg[M(z, E^{(i)})] dz \quad (6)$$

where the integration contour \mathcal{C}_{BZ} is the Brillouin zone $|z| = 1$ and $i = 1, 2$ is the band index. Although $E^{(i)}$ from the two bands are distinct and the M values are different, $W_{\text{BZ}}^{(1)} = W_{\text{BZ}}^{(2)}$ due to mode orthogonality. $W_{\text{BZ}}^{(i)} = 0$ or 1 corresponds to the absence or presence of a pair of topological edge states respectively [2, 58]. A similar form to Eq. (6) can be given for non-Hermitian sublattice symmetric models by replacing the integration contour with \mathcal{C}_{GBZ} , the GBZ associated with either one of the bands [8, 9, 60, 61].

We can interpret M on the Riemann sphere via the stereographic projection:

$$X(M) = \frac{2 \operatorname{Re}(M)}{|M|^2 + 1}, Y(M) = \frac{2 \operatorname{Im}(M)}{|M|^2 + 1}, Z(M) = \frac{|M|^2 - 1}{|M|^2 + 1} \quad (7)$$

where (X, Y, Z) are Cartesian coordinates of a point on the Riemann sphere. Below we refer to the sphere as defined by Eq. (7) as the M -Riemann sphere. $M(z, E^{(i)})$ in Eq. (6) defines the image of the bulk bands on the M -plane, denoted as $M(\mathcal{C}_{\text{BZ}})$ which can be plotted on the M -Riemann sphere. If the image of the two bands on the M -Riemann sphere each winds around the north-south pole axis, then the system supports a pair of topological edge states. In Fig. 1(b) we show $M(\mathcal{C}_{\text{BZ}})$ on the M -Riemann sphere for a trivial SSH and topological SSH model respectively. We see that it does not wind around the north-south pole axis of the M -Riemann sphere for the trivial case but does for the topological case. We also plot the OBC spectra for a finite $N = 32$ model and note that we have zero-energy edge states present only in the topological SSH, consistent with previous studies [2, 58].

Eq. (6) is not applicable for symmetry-broken systems. In Fig. 1(c) we consider several cases of such symmetry-broken Hermitian Hamiltonians. (The details of these Hamiltonians are provided in the SM Sec. I [57]). We see the presence of edge states even though the image of the two bands do not wind around the north-south pole axis. The observations here motivate us to develop a general

topological invariant that accounts for the existence of edge states in these symmetry-broken Hamiltonians.

The Hermitian invariant – We describe a topological invariant applicable to all gapped Hermitian models of Eq. (1). We introduce the concept of a *bulk eigenvector degeneracy*, which forms the basis of our invariant. From Eq. (4), at every E , in general there are four z solutions. An OBC eigenstate at energy E consists of a linear combination of these four solutions. Each (z, E) pair can be mapped to M using Eq. (5). At a given energy E , let us index the four M_i solutions with the corresponding z_i it was mapped from. A bulk eigenvector degeneracy is when $M_i = M_j \equiv M_{\text{deg}}$ but $i \neq j$. We show in SM Sec. III [57] that M_{deg} can be solved from:

$$M_{\text{deg}}^2 (t_{aa,1}t_{ba,-1} - t_{aa,-1}t_{ba,1}) + (t_{ab,1}t_{bb,-1} - t_{ab,-1}t_{bb,1}) + M_{\text{deg}} (t_{ab,1}t_{ba,-1} - t_{ab,-1}t_{ba,1} + t_{aa,1}t_{bb,-1} - t_{aa,-1}t_{bb,1}) = 0. \quad (8)$$

This is a quadratic equation and there are in general two M_{deg} solutions for our model.

We now generalize Eq. (6) as

$$W_{\text{BZ}}^{(i)} = \left(\sum_j \oint_{\mathcal{C}_{\text{BZ}}} \frac{d}{dz} \arg \left[M(z, E^{(i)}) - M_{\text{deg},j} \right] \frac{dz}{2\pi} \right) \text{mod } 2. \quad (9)$$

Each integral can be interpreted as a winding number of the image of a single band, i.e $M(\mathcal{C}_{\text{BZ}}^{(i)})$ around $M_{\text{deg},j}$ on the M -plane. The sum over j adds the contribution from each bulk degeneracy point. After taking mod 2, W_{BZ} can be 0 or 1. The total winding number W is defined as $W = W_{\text{BZ}}^{(1)} + W_{\text{BZ}}^{(2)}$ (without a mod 2). We claim that W corresponds to the number of (possibly non-zero energy) edge states, and the model under consideration can only have 0, 1 or 2 edge states.

For Hermitian models with sublattice-symmetric in off-diagonal form, M_{deg} is 0 or ∞ [60] and Eq. (9) reduces to Eq. (6). In symmetry-broken cases, M_{deg} can be arbitrary points $\in \mathbb{C}$ and different from 0 or ∞ . Examples of symmetry-broken cases for Hermitian are given in Fig. 1(c). The cases shown in Fig. 1(c) correspond to 0, 1 or 2 edge states. Calculating W from Eq. (9) amounts to counting how many $M(\mathcal{C}_{\text{BZ}})$ loop components can be contracted to a point on the M -Riemann sphere without touching M_{deg} . These correspond to $W = 0, 1$, and 2 in Fig. 1(c) respectively, which also correspond to the number of edge states in the OBC.

The general invariant – Eq. (9) only works in the Hermitian case where the GBZ reduces to the BZ. In generic non-Hermitian systems, the GBZ may have a different topology, possibly leading to nontrivial braiding of the OBC bands [51, 52] or disconnected components of the GBZ [59]. We now present the following invariant that determines edge states of generic models in the form of Eq. (1) regardless of the underlying GBZ topology. We

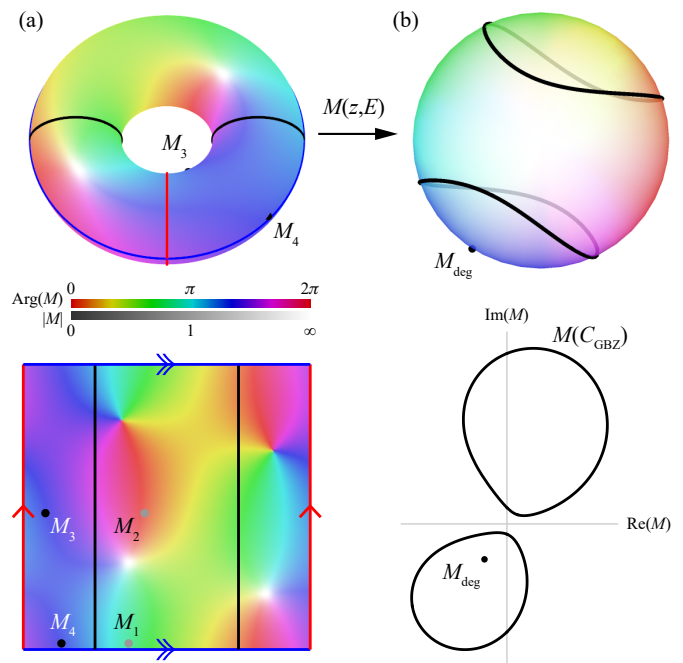


FIG. 2. General invariant as a winding number resulting from the mapping between Riemann surfaces. The Hamiltonian is the same as Fig. 1(c), middle panel. (a) Top panel: Band structure Riemann surface as a torus, colored by M values where the color gives $\arg(M)$ and the brightness gives $|M|$. Black curves are the GBZ on the torus. Bottom panel: planar representation of the torus by cutting along the red and blue circles. The set of M values for the only edge state in the model, where $M_3 = M_4$, have been marked on the plane and on the torus (M_3 and M_4 only). (b) Top panel: The M -Riemann sphere with the $M_{\text{deg}} = M_3 = M_4$ (black dot) point and the $M(\mathcal{C}_{\text{GBZ}})$ (black curves). Bottom: Representation on the M plane, showing the $M(\mathcal{C}_{\text{GBZ}})$ and the M_{deg} point.

define

$$W_j \equiv \left(1 + \frac{1}{2\pi i} \int_{M(\mathcal{C}_{\text{GBZ}})} dM \frac{d}{dM} \ln \frac{M - M_{\text{deg},j}}{M - M_{\text{branch}}} \right) \text{mod } 2 \quad (10)$$

where M_{branch} are the M -plane branch points (see SM Sec. II [57]). An $M_{\text{deg},j}$ point corresponds to an edge state if $W_j = 1$. The total number of edge states is $W = W_1 + W_2$, and reduces to Eq. (9) for Hermitian systems.

Sketch of the proof– We now provide a sketch of the proof of Eqs. (9) and (10) by considering the analytical condition for edge states in the OBC for a finite chain with N unit cells. For a model described by Eq. (1) subject to the OBC, in order to have a state at an energy E , the following condition must be satisfied (see SM

Sec. V [57]):

$$\left| \begin{array}{cc} M_1 & M_2 \\ 1 & 1 \end{array} \right| \left| \begin{array}{cc} M_3 & M_4 \\ 1 & 1 \end{array} \right| - \left| \begin{array}{cc} M_1 & M_3 \\ 1 & 1 \end{array} \right| \left| \begin{array}{cc} M_2 & M_4 \\ 1 & 1 \end{array} \right| \left(\frac{z_2}{z_3} \right)^N + \dots = 0. \quad (11)$$

If Eq. (11) holds in the thermodynamic limit $N \rightarrow \infty$, the leading terms shown here must vanish. One way to do so is to have $|z_2| = |z_3|$. These are the bulk states as the phases of z_2 and z_3 are unspecified leading to a continuum set of solutions that form the GBZ. The other way is to have $M_1 = M_2$ or $M_3 = M_4$ so that the leading term is zero. These lead to states with discrete and isolated energy, which are the edge states.

We note that $M_1 = M_2$ or $M_3 = M_4$ are two possible but not all cases of M_{deg} , as one can also have e.g. $M_1 = M_3$. Eqs. (9) and (10) can be interpreted as an index tracker. When the winding number is nontrivial, the M_{deg} points have the correct indices i in M_i that lead to edge states. The indices of the M_{deg} points are related to the GBZ. Since the GBZ is defined by $|z_2| = |z_3|$, on the band structure Riemann sphere (Fig 2(a)), z_1 and z_2 will always be on the opposite side of the GBZ as compared with z_3 and z_4 . Consider now the indices associated with the M_{deg} point. As an example, suppose with certain parameters of the Hamiltonian this M_{deg} point corresponds to $M_1 = M_3$. If we vary the parameters of the Hamiltonian, this M_{deg} point may cross $M(\mathcal{C}_{\text{GBZ}})$, the image of the GBZ on the M -sphere. When the crossing occurs, however, the labeling of the z values must change between z_2 and z_3 , and therefore the indices associated with the M_{deg} point much change such that it now corresponds to $M_1 = M_2$. The crossing therefore indicates the emergence of an edge state from the bulk state as defined by the GBZ.

The proof of Eq. (10) formalizes the above argument by defining the *inside of the GBZ*, consisting of states where the z 's are two roots of Eq. (4) with the smallest amplitudes (i.e. z_1 or z_2). The inside of the GBZ is considered as a region on the Riemann surface of the band structure, which is then analytically mapped to the M -Riemann sphere through Eq. (5) (Fig. 2). The M_{deg} point on the sphere will be covered twice by the GBZ inside if $M_1 = M_2$, zero times if $M_3 = M_4$, and exactly once for all other cases. By defining a winding integral on the band structure Riemann surface and mapping it to the M -Riemann sphere, the number of times the GBZ inside covers a region can be expressed as an M winding number. The argument above directly leads to Eq. (9), applicable for Hermitian models. For non-Hermitian models, the $M(\mathcal{C}_{\text{GBZ}})$ loops may merge or intersect with each other, and it becomes necessary to take into account the contour direction used for integration. However, since the winding direction may be reversed in the mapping process, we need to modify the raw winding number by subtracting the winding number of M_{branch} , whose preimages are degenerate and therefore always on the same side of the GBZ. Complete proofs for Eqs. (10)

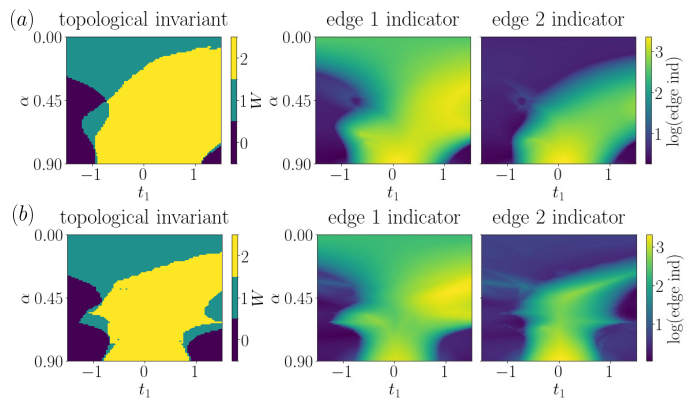


FIG. 3. (a) Topological invariant calculated from Eq. (9) and edge state indicators for finite chain with $N = 32$ for 6400 models for a linear combination of a Hermitian random model and a Hermitian SSH model, where α is a weighting parameter. (b) Topological invariant calculated from Eq. (10) and edge state indicators for finite chain with $N = 32$ for 6400 models for a linear combination of a non-Hermitian random model and a Hermitian SSH model. Full parameters in SM Sec. I [57].

and (9) can be found in SM Sec. VI and VII [57], respectively.

Numerical results – We numerically demonstrate both the Hermitian invariant Eq. (9) and the general invariant in Eq. (10) by calculating the number of edge states predicted by the invariants and an *edge state indicator* on the OBC eigenstates of a finite $N = 32$ chain in Fig. 3. We use a randomly chosen Hermitian and non-Hermitian model for Fig. 3(a) and Fig. 3(b) respectively called H_h and H_{nh} (full parameters given in SM Sec. I [57]). In Fig. 3(a), we define $H(z) = (1 - \alpha)H_h + \alpha H_{ssh}$, varying α from 0 to 0.90 and t_1 in the SSH Hamiltonian from -1.5 to 1.5 over 80 steps, resulting in 6400 models. We do a similar construction, except with the use of H_{nh} for Fig. 3(b). The topological invariants are shown on the left in Fig. 3. They are calculated by finding $M(\mathcal{C}_{\text{GBZ}})$ and counting $M_{\text{deg},j}$ (and M_{branch} for the general invariant) inside the $M(\mathcal{C}_{\text{GBZ}})$ curves as dictated by Eq. (9) and Eq. (10). For Hermitian systems, one could use the inverse-participation ratio (IPR) for numerically detecting edge states [62]. For non-Hermitian systems however, bulk states are also localized, complicating the use of IPR to distinguish edge states. We introduce a new edge state indicator which is calculated from distances between each OBC mode in $\{\text{Re}(E), \text{Im}(E), |\text{Im}(k_2) - \text{Im}(k_3)|\}$ space and which has no connection to Eq. (9) and Eq. (10) and use it for both the Hermitian and non-Hermitian cases. We see that our edge-state invariant matches the edge state indicator of the OBC chains very well, verifying the validity of Eq. (9) and Eq. (10). More detail on these numerical tests and animations of a slice of the phase diagrams can be found in SM Sec. IV [57].

Discussion – Unlike many symmetry-protected topological invariants [2, 8, 9], both Eq. (9) and Eq. (10) re-

mains unchanged under z -independent unitary and similarity transformations of the Hamiltonian. Such transformations correspond to Möbius transformations on the M -Riemann sphere [60], which preserves cross-ratios and leaves the invariant unchanged. This invariance aligns with the physical intuition that edge states should be unaffected by such transformations as both the bulk spectral properties and the OBC are unaffected.

The topological invariants we provide in this work are applicable to systems that are traditionally defined as a topological or trivial phase in symmetry-protected classifications [2]. Within the context of our models of Eq. (1), they are a broader invariant that applies to non-zero energy edge states and the emergence of which does not coincide with the gap closing condition (see SM Sec. VIII [57]). Our work is related but distinct from several recent works defining a topological invariant without symmetry constraints using Green's function poles [35, 37, 63–65] which requires a Green's function of a finite system. In contrast, our invariant is calculated purely from bulk quantities. The bulk degeneracy points cannot be created or destroyed for general cases of Eq. (1), which gives the edge states associated with the bulk eigenvector degeneracies a topological origin under

our formalism in Eq. (9) and Eq. (10).

In conclusion, we have derived new topological invariants that apply to symmetry-broken and symmetry-protected nearest-neighbor two-band models with arbitrary complex couplings. Our work demonstrates that the full complex band structure [11, 37, 59, 61, 66–78] is fundamental not only for non-Hermitian systems but also for Hermitian ones. Our understanding of the topological origins of edge states in this class of symmetry-breaking models may generalize to other Hermitian and non-Hermitian models [2, 79–88].

J.Z. thanks Prof. Zhong Wang for helpful discussions at an early stage of this work. This work is supported by a Simons Investigator in Physics grant from the Simons Foundation (Grant No. 827065), and by a MURI grant from the U. S. Air Force Office of Scientific Research (Grant No. FA9550-22-1-0339). The work of A.N.P. has been supported by research grants from the Center for New Scientists and from the Center for Scientific Excellence at the Weizmann Institute of Science, by the Quantum Science and Technology Program of the Israel Council for Higher Education and by the Minerva Foundation. J.Z. was funded in part by the Fulbright Future Scholarship.

-
- [1] M. Z. Hasan and C. L. Kane, Colloquium: Topological insulators, *Rev. Mod. Phys.* **82**, 3045 (2010).
- [2] C.-K. Chiu, J. C. Y. Teo, A. P. Schnyder, and S. Ryu, Classification of topological quantum matter with symmetries, *Rev. Mod. Phys.* **88**, 035005 (2016).
- [3] J. Cayssol and J. N. Fuchs, Topological and geometrical aspects of band theory, *Journal of Physics: Materials* **4**, 034007 (2021), [arXiv:2012.11941 \[cond-mat.mes-hall\]](#).
- [4] A. Alase, E. Cobanera, G. Ortiz, and L. Viola, Wiener-Hopf factorization approach to a bulk-boundary correspondence and stability conditions for topological zero-energy modes, *Annals of Physics* **458**, 169457 (2023), [arXiv:2304.03524 \[cond-mat.stat-mech\]](#).
- [5] A. Altland and M. R. Zirnbauer, Nonstandard symmetry classes in mesoscopic normal-superconducting hybrid structures, *Phys. Rev. B* **55**, 1142 (1997).
- [6] A. Kitaev, Periodic table for topological insulators and superconductors, *AIP Conference Proceedings* **1134** (2009).
- [7] S. Ryu, A. P. Schnyder, A. Furusaki, and A. W. W. Ludwig, Topological insulators and superconductors: tenfold way and dimensional hierarchy, *New Journal of Physics* **12**, 065010 (2010), [arXiv:0912.2157 \[cond-mat.mes-hall\]](#).
- [8] S. Yao and Z. Wang, Edge States and Topological Invariants of non-Hermitian Systems, *Phys. Rev. Lett.* **121**, 086803 (2018).
- [9] K. Yokomizo and S. Murakami, Non-Bloch Band Theory of non-Hermitian Systems, *Phys. Rev. Lett.* **123**, 066404 (2019).
- [10] Y. Ashida, Z. Gong, and M. Ueda, non-Hermitian physics, *Advances in Physics* **69**, 249 (2020), [arXiv:2006.01837 \[cond-mat.mes-hall\]](#).
- [11] C. H. Lee and R. Thomale, Anatomy of skin modes and topology in non-Hermitian systems, *Phys. Rev. B* **99**, 201103 (2019), [arXiv:1809.02125 \[cond-mat.other\]](#).
- [12] F. K. Kunst, E. Edvardsson, J. C. Budich, and E. J. Bergholtz, Biorthogonal bulk-boundary correspondence in non-Hermitian systems, *Phys. Rev. Lett.* **121**, 026808 (2018).
- [13] E. J. Bergholtz, J. C. Budich, and F. K. Kunst, Exceptional topology of non-Hermitian systems, *Rev. Mod. Phys.* **93**, 015005 (2021).
- [14] K. Ding, C. Fang, and G. Ma, Non-Hermitian topology and exceptional-point geometries, *Nature Reviews Physics* **4**, 745 (2022), [arXiv:2204.11601 \[quant-ph\]](#).
- [15] R. Lin, T. Tai, L. Li, and C. H. Lee, Topological non-Hermitian skin effect, *Frontiers of Physics* **18**, 53605 (2023), [arXiv:2302.03057 \[cond-mat.mes-hall\]](#).
- [16] K. Kawabata, K. Shiozaki, M. Ueda, and M. Sato, Symmetry and Topology in non-Hermitian Physics, *Phys. Rev. X* **9**, 041015 (2019).
- [17] H. Zhou and J. Y. Lee, Periodic table for topological bands with non-Hermitian symmetries, *Phys. Rev. B* **99**, 235112 (2019).
- [18] Z.-W. Zuo and D. Kang, Reentrant localization transition in the Su-Schrieffer-Heeger model with random-dimer disorder, *Phys. Rev. A* **106**, 013305 (2022).
- [19] T. Kawarabayashi and Y. Hatsugai, Bulk-edge correspondence with generalized chiral symmetry, *Phys. Rev. B* **103**, 205306 (2021).
- [20] S. Verma and M. J. Park, Non-bloch band theory of subsymmetry-protected topological phases, *Phys. Rev. B* **110**, 035424 (2024).
- [21] L. Li and S. Chen, Hidden-symmetry-protected topological phases on a one-dimensional lattice, *EPL (Europhysics Letters)* **109**, 40006 (2015), [arXiv:1411.0260](#)

- [cond-mat.str-el].
- [22] R. Chaunsali, H. Xu, J. Yang, P. G. Kevrekidis, and G. Theoharis, Stability of topological edge states under strong nonlinear effects, *Phys. Rev. B* **103**, 024106 (2021).
- [23] E. G. Cinnirella, A. Nava, G. Campagnano, and D. Giuliano, Fate of high winding number topological phases in the disordered extended su-schrieffer-heeger model, *Phys. Rev. B* **109**, 035114 (2024).
- [24] H.-C. Hsu and T.-W. Chen, Topological Anderson insulating phases in the long-range Su-Schrieffer-Heeger model, *Phys. Rev. B* **102**, 205425 (2020).
- [25] B. Pérez-González, M. Bello, A. Gómez-León, and G. Platero, Interplay between long-range hopping and disorder in topological systems, *Phys. Rev. B* **99**, 035146 (2019).
- [26] A. Bissonnette, N. Delnour, A. McKenna, H. Eleuch, M. Hilke, and R. MacKenzie, Boundary-induced topological transition in an open Su-Schrieffer-Heeger model, *Phys. Rev. B* **109**, 075106 (2024).
- [27] V. Kachin, J. C. L. Carreño, and M. Stobińska, Ultra-robust topologically protected edge states in quasi-1d systems, *arXiv preprint arXiv:2401.07137* (2024).
- [28] S. Longhi, Probing one-dimensional topological phases in waveguide lattices with broken chiral symmetry, *Optics Letters* **43**, 4639 (2018).
- [29] Z. Wang, X. Wang, Z. Hu, D. Bongiovanni, D. Jukić, L. Tang, D. Song, R. Morandotti, Z. Chen, and H. Buljan, Sub-symmetry-protected topological states, *Nature Physics* **19**, 992 (2023), [arXiv:2205.07285 \[physics.optics\]](#).
- [30] M. Kang, M. Lee, and S. Cheon, Subsymmetry protected topology in topological insulators and superconductors, *Phys. Rev. Res.* **6**, 033323 (2024).
- [31] S. Saha, T. Nag, and S. Mandal, Topological characterization of special edge modes from the winding of relative phase (2023), [arXiv:2306.08100 \[cond-mat.mes-hall\]](#).
- [32] S. Liu, S. Ma, R. Shao, L. Zhang, B. Yang, M. Navarro-Cía, T. J. Cui, and S. Zhang, Edge state mimicking topological behavior in a one-dimensional electrical circuit, *New Journal of Physics* **23**, 103005 (2021).
- [33] M. Pletyukhov, D. M. Kennes, J. Klinovaja, D. Loss, and H. Schoeller, Surface charge theorem and topological constraints for edge states: Analytical study of one-dimensional nearest-neighbor tight-binding models, *Phys. Rev. B* **101**, 165304 (2020).
- [34] M. Pletyukhov, D. M. Kennes, J. Klinovaja, D. Loss, and H. Schoeller, Topological invariants to characterize universality of boundary charge in one-dimensional insulators beyond symmetry constraints, *Phys. Rev. B* **101**, 161106 (2020).
- [35] N. Müller, K. Piasotski, D. M. Kennes, H. Schoeller, and M. Pletyukhov, Universal properties of boundary and interface charges in multichannel one-dimensional models without symmetry constraints, *Phys. Rev. B* **104**, 125447 (2021).
- [36] S. Miles, D. M. Kennes, H. Schoeller, and M. Pletyukhov, Universal properties of boundary and interface charges in continuum models of one-dimensional insulators, *Phys. Rev. B* **104**, 155409 (2021).
- [37] J.-W. Rhim, J. H. Bardarson, and R.-J. Slager, Unified bulk-boundary correspondence for band insulators, *Phys. Rev. B* **97**, 115143 (2018).
- [38] V. M. Martínez Alvarez, J. E. Barrios Vargas, and L. E. F. Foa Torres, Non-hermitian robust edge states in one dimension: Anomalous localization and eigenspace condensation at exceptional points, *Phys. Rev. B* **97**, 121401 (2018).
- [39] H.-Q. Liang and L. Li, Topological properties of non-Hermitian Creutz ladders, *Chinese Physics B* **31**, 010310 (2022), [arXiv:2108.12836 \[quant-ph\]](#).
- [40] Y. Z. Han, J. S. Liu, and C. S. Liu, The topological counterparts of non-Hermitian SSH models, *New Journal of Physics* **23**, 123029 (2021), [arXiv:2103.12397 \[quant-ph\]](#).
- [41] S. Lieu, Topological phases in the non-Hermitian su-schrieffer-heeger model, *Phys. Rev. B* **97**, 045106 (2018).
- [42] D. Halder, R. Thomale, and S. Basu, Circuit realization of a two-orbital non-hermitian tight-binding chain, *Phys. Rev. B* **109**, 115407 (2024).
- [43] D. Halder, S. Ganguly, and S. Basu, Properties of the non-Hermitian SSH model: role of {PT} symmetry, *Journal of Physics Condensed Matter* **35**, 105901 (2023), [arXiv:2209.13838 \[quant-ph\]](#).
- [44] C. Yuce, Topological phase in a non-Hermitian PT symmetric system, *Physics Letters A* **379**, 1213 (2015), [arXiv:1502.07160 \[quant-ph\]](#).
- [45] W. P. Su, J. R. Schrieffer, and A. J. Heeger, Solitons in polyacetylene, *Phys. Rev. Lett.* **42**, 1698 (1979).
- [46] T. E. Lee, Anomalous edge state in a non-Hermitian lattice, *Phys. Rev. Lett.* **116**, 133903 (2016).
- [47] D. S. Borgnia, A. J. Kruchkov, and R.-J. Slager, non-Hermitian Boundary Modes and Topology, *Phys. Rev. Lett.* **124**, 056802 (2020).
- [48] S. Longhi, Probing non-Hermitian skin effect and non-Bloch phase transitions, *Phys. Rev. Research* **1**, 023013 (2019).
- [49] G.-F. Guo, X.-X. Bao, and L. Tan, Non-Hermitian bulk-boundary correspondence and singular behaviors of generalized Brillouin zone, *New Journal of Physics* **23**, 123007 (2021).
- [50] E. McCann, Catalog of noninteracting tight-binding models with two energy bands in one dimension, *Phys. Rev. B* **107**, 245401 (2023).
- [51] Y. Fu and Y. Zhang, Braiding topology of non-hermitian open-boundary bands, *Phys. Rev. B* **110**, L121401 (2024).
- [52] Y. Li, X. Ji, Y. Chen, X. Yan, and X. Yang, Topological energy braiding of non-Bloch bands, *Phys. Rev. B* **106**, 195425 (2022).
- [53] C. C. Wojcik, X.-Q. Sun, T. c. v. Bzdušek, and S. Fan, Homotopy characterization of non-Hermitian Hamiltonians, *Phys. Rev. B* **101**, 205417 (2020).
- [54] H. Hu and E. Zhao, Knots and non-Hermitian Bloch Bands, *Phys. Rev. Lett.* **126**, 010401 (2021).
- [55] Z. Li and R. S. K. Mong, Homotopical characterization of non-Hermitian band structures, *Phys. Rev. B* **103**, 155129 (2021).
- [56] K. Yang, Z. Li, J. L. K. König, L. Røddland, M. Stålhammar, and E. J. Bergholtz, Homotopy, symmetry, and non-Hermitian band topology, *Reports on Progress in Physics* **87**, 078002 (2024), [arXiv:2309.14416 \[cond-mat.mes-hall\]](#).
- [57] See Supplemental Material, URL will be inserted by publisher for additional proofs and derivations of main equations as well as animations of phase diagram slices.
- [58] J. K. Asbóth, O. László, and P. András, A short course on topological insulators, *Lecture Notes in Physics* **919**, 10.1007/978-3-319-25607-8 (2016).

- [59] H. Wang, J. Zhong, and S. Fan, Non-Hermitian photonic band winding and skin effects: a tutorial, *Advances in Optics and Photonics* **16**, 659 (2024).
- [60] J. Zhong, H. Wang, and S. Fan, Pole and zero edge state invariant for 1d non-Hermitian sublattice symmetry (2024), [arXiv:2410.11257 \[cond-mat.mes-hall\]](https://arxiv.org/abs/2410.11257).
- [61] Z. Yang, K. Zhang, C. Fang, and J. Hu, non-Hermitian bulk-boundary correspondence and auxiliary generalized Brillouin zone theory, *Phys. Rev. Lett.* **125**, 226402 (2020).
- [62] S. Ganeshan, J. H. Pixley, and S. Das Sarma, Nearest neighbor tight binding models with an exact mobility edge in one dimension, *Phys. Rev. Lett.* **114**, 146601 (2015).
- [63] K. Esaki, M. Sato, K. Hasebe, and M. Kohmoto, Edge states and topological phases in non-Hermitian systems, *Phys. Rev. B* **84**, 205128 (2011).
- [64] S. Tamura, S. Hoshino, and Y. Tanaka, Generalization of spectral bulk-boundary correspondence, *Phys. Rev. B* **104**, 165125 (2021).
- [65] K. Piasotski, N. Müller, D. M. Kennes, H. Schoeller, and M. Pletyukhov, Universal properties of boundary and interface charges in multichannel one-dimensional continuum models, *Phys. Rev. B* **106**, 165405 (2022).
- [66] M. Pletyukhov, D. M. Kennes, J. Klinovaja, D. Loss, and H. Schoeller, Surface charge theorem and topological constraints for edge states: Analytical study of one-dimensional nearest-neighbor tight-binding models, *Phys. Rev. B* **101**, 165304 (2020).
- [67] A. Alase, E. Cobanera, G. Ortiz, and L. Viola, Generalization of Bloch's theorem for arbitrary boundary conditions: Theory, *Phys. Rev. B* **96**, 195133 (2017).
- [68] H. Wang, L. Fan, and S. Fan, One-dimensional non-Hermitian band structures as Riemann surfaces, *Phys. Rev. A* **110**, 012209 (2024).
- [69] F. K. Kunst and V. Dwivedi, Non-Hermitian systems and topology: A transfer-matrix perspective, *Phys. Rev. B* **99**, 245116 (2019).
- [70] V. Gurarie, Single-particle Green's functions and interacting topological insulators, *Phys. Rev. B* **83**, 085426 (2011).
- [71] I. C. Fulga, F. Hassler, and A. R. Akhmerov, Scattering theory of topological insulators and superconductors, *Phys. Rev. B* **85**, 165409 (2012).
- [72] A. Montag, A. Felski, and F. K. Kunst, Topological Order in the Spectral Riemann Surfaces of Non-Hermitian Systems, [arXiv e-prints](https://arxiv.org/abs/2410.18616), [arXiv:2410.18616 \[quant-ph\]](https://arxiv.org/abs/2410.18616).
- [73] Y.-M. Hu and Z. Wang, Green's functions of multiband non-Hermitian systems, *Phys. Rev. Res.* **5**, 043073 (2023).
- [74] E. Prodan, Analytic structure of Bloch functions for linear molecular chains, *Phys. Rev. B* **73**, 035128 (2006).
- [75] W. Kohn, Analytic properties of Bloch waves and Wannier functions, *Phys. Rev.* **115**, 809 (1959).
- [76] M. G. Reuter, A unified perspective of complex band structure: interpretations, formulations, and applications, *J. Phys. Condens. Matter* **29**, 053001 (2017), [arXiv:1607.06724 \[cond-mat.mtrl-sci\]](https://arxiv.org/abs/1607.06724).
- [77] Y.-M. Hu, H.-Y. Wang, Z. Wang, and F. Song, Geometric origin of non-bloch \mathcal{PT} symmetry breaking, *Phys. Rev. Lett.* **132**, 050402 (2024).
- [78] Y. Hatsugai, Edge states in the integer quantum hall effect and the Riemann surface of the Bloch function, *Phys. Rev. B* **48**, 11851 (1993).
- [79] Y. Long, Z. Wang, C. Zhang, H. Xue, Y. X. Zhao, and B. Zhang, Non-Abelian braiding of topological edge bands, *Phys. Rev. Lett.* **132**, 236401 (2024).
- [80] R. Verresen, N. G. Jones, and F. Pollmann, Topology and edge modes in quantum critical chains, *Phys. Rev. Lett.* **120**, 057001 (2018).
- [81] S. Longhi, Non-Hermitian Gauged Topological Laser Arrays, *Annalen der Physik* **530**, 1800023 (2018), [arXiv:1801.00996 \[physics.optics\]](https://arxiv.org/abs/1801.00996).
- [82] P. St-Jean, V. Goblot, E. Galopin, A. Lemaitre, T. Ozawa, L. Le Gratiet, I. Sagnes, J. Bloch, and A. Amo, Lasing in topological edge states of a one-dimensional lattice, *Nature Photonics* **11**, 651 (2017), [arXiv:1704.07310 \[cond-mat.mes-hall\]](https://arxiv.org/abs/1704.07310).
- [83] A. Y. Kitaev, Unpaired Majorana fermions in quantum wires, *Physics-uspekhi* **44**, 131 (2001).
- [84] A. Stern and N. H. Lindner, Topological Quantum Computation—From Basic Concepts to First Experiments, *Science* **339**, 1179 (2013).
- [85] L. Lu, J. D. Joannopoulos, and M. Soljačić, Topological photonics, *Nature photonics* **8**, 821 (2014).
- [86] M. Xiao, Z. Q. Zhang, and C. T. Chan, Surface impedance and bulk band geometric phases in one-dimensional systems, *Phys. Rev. X* **4**, 021017 (2014).
- [87] E. Tang, J. Agudo-Canalejo, and R. Golestanian, Topology protects chiral edge currents in stochastic systems, *Phys. Rev. X* **11**, 031015 (2021).
- [88] X. Ni, S. Yves, A. Krasnok, and A. Alú, Topological metamaterials, *Chemical Reviews* **123**, 7585 (2023).
- [89] K. Kawabata, N. Okuma, and M. Sato, Non-Bloch band theory of non-Hermitian Hamiltonians in the symplectic class, *Phys. Rev. B* **101**, 195147 (2020).
- [90] Y. Fu and Y. Zhang, Anatomy of open-boundary bulk in multiband non-Hermitian systems, *Phys. Rev. B* **107**, 115412 (2023).
- [91] S. Shi, S. Chu, Y. Xie, and Y. Chen, Machine learning topological energy braiding of non-bloch bands, [arXiv preprint arXiv:2408.01141](https://arxiv.org/abs/2408.01141) (2024).
- [92] J. Chen, Z. Wang, Y.-T. Tan, C. Wang, and J. Ren, Machine learning of knot topology in non-Hermitian band braids, *Communications Physics* **7**, 209 (2024), [arXiv:2401.10908 \[cond-mat.mes-hall\]](https://arxiv.org/abs/2401.10908).
- [93] Y. Yu, L.-W. Yu, W. Zhang, H. Zhang, X. Ouyang, Y. Liu, D.-L. Deng, and L. M. Duan, Experimental unsupervised learning of non-Hermitian knotted phases with solid-state spins, *npj Quantum Information* **8**, 116 (2022), [arXiv:2112.13785 \[quant-ph\]](https://arxiv.org/abs/2112.13785).
- [94] Y. Long, H. Xue, and B. Zhang, Unsupervised Learning of Topological Non-Abelian Braiding in Non-Hermitian Bands, [arXiv e-prints](https://arxiv.org/abs/2401.17968), [arXiv:2401.17968 \[cond-mat.mes-hall\]](https://arxiv.org/abs/2401.17968).
- [95] L.-W. Yu and D.-L. Deng, Unsupervised learning of non-Hermitian topological phases, *Phys. Rev. Lett.* **126**, 240402 (2021).
- [96] R. Beals, R. Wong, *et al.*, *Explorations in complex functions*, Vol. 287 (Springer, 2020).
- [97] Z. Gong, Y. Ashida, K. Kawabata, K. Takasan, S. Higashikawa, and M. Ueda, Topological Phases of non-Hermitian Systems, *Phys. Rev. X* **8**, 031079 (2018).
- [98] H. Jiang, C. Yang, and S. Chen, Topological invariants and phase diagrams for one-dimensional two-band non-Hermitian systems without chiral symmetry, *Phys. Rev. A* **98**, 052116 (2018).

SUPPLEMENTARY MATERIAL

When giving model parameters in this Supplementary Material (SM), it is convenient to write Eq. (1) in the form:

$$H(z) = h_- z^{-1} + h_0 + h_+ z \quad (\text{S1})$$

where

$$h_- = \begin{bmatrix} t_{aa,-1} & t_{ab,-1} \\ t_{ba,-1} & t_{bb,-1} \end{bmatrix}, h_0 = \begin{bmatrix} t_{aa,0} & t_{ab,0} \\ t_{ba,0} & t_{bb,0} \end{bmatrix}, h_+ = \begin{bmatrix} t_{aa,1} & t_{ab,1} \\ t_{ba,1} & t_{bb,1} \end{bmatrix}. \quad (\text{S2})$$

I. MODEL PARAMETERS FOR FIGS. 1 AND 3

The models used in Figs. 1 and 3 involve the following:

Model	h_-		h_0		h_+	
H_h	$0.84 - 0.14i$	$0.02 - 0.69i$	$-0.66 + 0.00i$	$-0.96 - 0.80i$	$0.84 + 0.14i$	$0.02 + 0.69i$
	$0.02 - 0.69i$	$-0.82 - 0.60i$	$-0.96 + 0.80i$	$-0.58 + 0.00i$	$0.02 + 0.69i$	$-0.82 + 0.60i$
H_{nh}	$0.74 - 0.13i$	$-0.79 - 0.84i$	$-0.18 + 0.32i$	$-0.44 - 0.84i$	$0.51 + 0.4i$	$-0.86 + 0.4i$
	$-0.43 - 0.08i$	$0.01 + 0.6i$	$-0.33 + 0.7i$	$0.21 - 0.74i$	$-0.44 + 0.38i$	$-0.86 - 0.03i$
H_{ssh}		$0 \ t_2$		$0 \ t_1$		$0 \ 0$
		$0 \ 0$		$t_1 \ 0$		$t_2 \ 0$

TABLE I. Model parameters used in Figs. 1 and 3.

In Fig. 1(b) we use $H = H_{ssh}$ with $t_1 = 1.5, 0.5$ respectively and $t_2 = 1$ for both sub-plots. In Fig. 1(c) we use

$$H = (1 - \alpha)H_h + \alpha H_{ssh} \quad (\text{S3})$$

where $t_1 = 1.5, t_2 = 1, \alpha = 0.85$ for the no edge state case, $\alpha = 0$ for the one edge state case and $t_1 = 0.5, t_2 = 1, \alpha = 0.5$ for the two edge state case. The parameters for these cases are within the parameter ranges for the phase diagram in Fig. 3(a). Fig. 3(a), we use $t_2 = 1$ for the SSH parameter and vary α and t_1 . In Fig. 3(b) we use

$$H = (1 - \alpha)H_{nh} + \alpha H_{ssh}, \quad (\text{S4})$$

where we again use $t_2 = 1$ for the SSH parameter and vary α and t_1 .

II. EIGENVALUE AND EIGENVECTOR RIEMANN SURFACE

The equations in Eq. (4) and Eq. (5) can be viewed as Riemann surfaces [11, 59, 61, 68, 69, 73–76]. We use the underlying algebraic structure of these Riemann surfaces for our derivations such as the derivation for M_{deg} (SM Sec. III) and our edge-state invariants (SM Sec. VII and VI). However, the many different projections of these Riemann surfaces, along with the branch points in the z -plane (relevant to the eigenvalue topology – see SM Sec. VIII), E -plane, and M -plane (relevant to the general edge-state invariant – see SM Sec. VI), can be potentially confusing.

Here, we give a glossary of these concepts. The eigenvalue Riemann surface (or band structure Riemann surface) is described by the set of $(E, z) \in \mathbb{C}^2$ given by $f(E, z) = 0$. Here, $f(E, z)$ is Eq. (4) converted into a polynomial in both z and E . For a general model of Eq. (1) this polynomial has degree 4 in z and degree 2 in E . The eigenvector Riemann surface is derived using Eq. (5) where $M \in \mathbb{C}$. By substituting E from Eq. (4) into Eq. (5), we can write an equation that is a polynomial in both M and z :

$$g(M, z) = -t_{ab,-1} - z(t_{ab,0} + t_{ab,+1}z) + M^2(t_{ba,-1} + z(t_{ba,0} + t_{ba,+1}z)) + M(-t_{aa,-1} + t_{bb,-1} + z(-t_{aa,0} + t_{bb,0} - t_{aa,+1}z + t_{bb,+1}z))$$

This is a polynomial of degree 2 in both M and z . The set of $(M, z) \in \mathbb{C}^2$ satisfying $g(M, z) = 0$ gives the eigenvector Riemann surface. Both $g(M, z) = 0$ and $f(E, z) = 0$ define valid Riemann surfaces because the partial derivatives $\frac{\partial g}{\partial M}, \frac{\partial g}{\partial z}$ and $\frac{\partial f}{\partial E}, \frac{\partial f}{\partial z}$ respectively do not vanish simultaneously in general. However, there are instances where models

of the form given in Eq. (1) may fail to describe smooth Riemann surfaces [59, 89]. Such cases are excluded when we refer to the ‘general’ scenario of our model.

We can rearrange $f(E, z) = 0, g(M, z) = 0$ to get an equation of $h(E, M) = 0$, which is a polynomial in both E and M . For general models, $h(E, M) = 0$ does not define a valid Riemann surface, as the partial derivatives $\frac{\partial h}{\partial E}$ and $\frac{\partial h}{\partial M}$ both vanish at the bulk eigenvector degeneracy points. Nevertheless, the visualization of the $M(E)$ and $E(M)$ sheets may be useful (and we use the $M(E)$ sheets in SM Sec. IX).

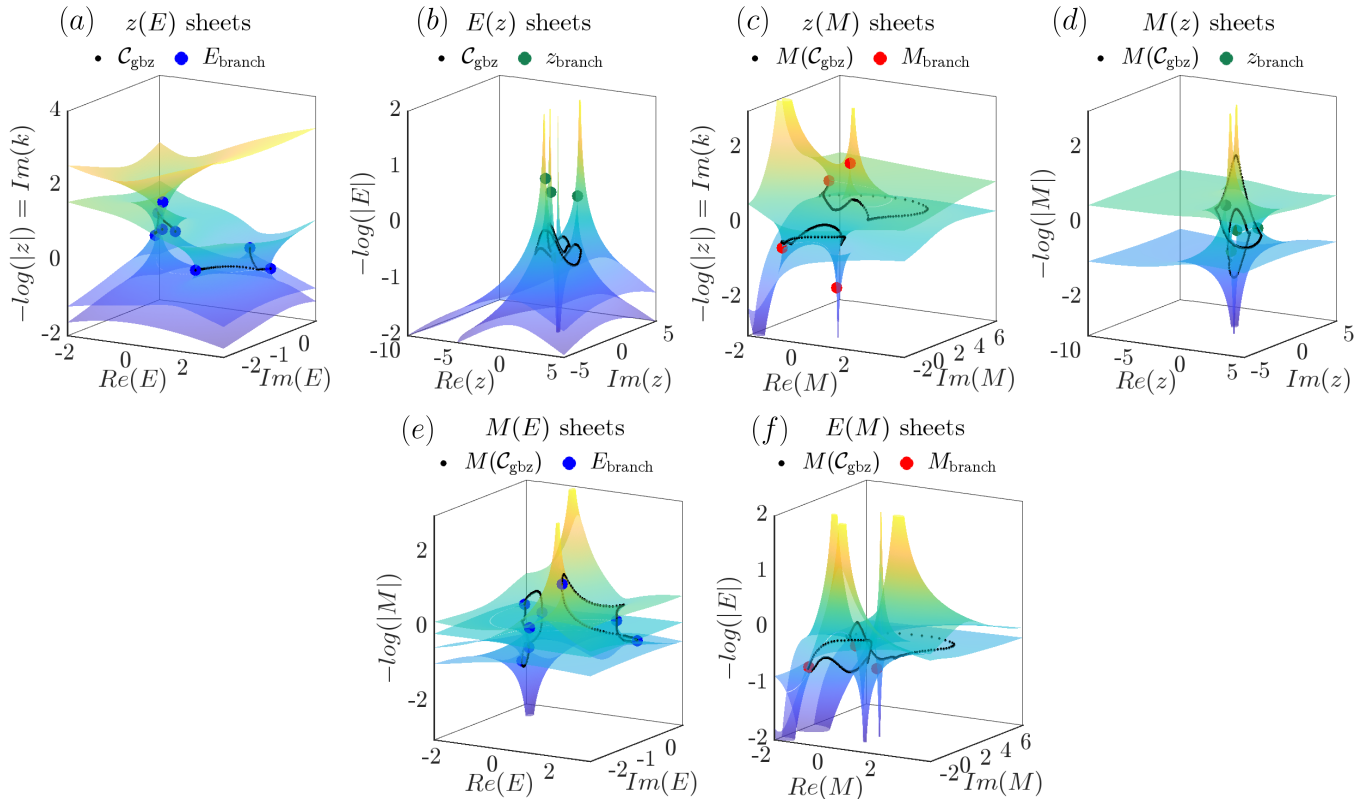


FIG. S1. In general, the nearest-neighbour (between unit cells) two-band tight-binding model in Eq. (1) will have (a) four $z(E)$ sheets with eight E branch points (b) two $E(z)$ sheets with four z branch points (c) two $z(M)$ sheets with four M branch points (d) two $M(z)$ sheets (e) four $M(E)$ sheets and (f) two $E(M)$ sheets. These Riemann sheets are for the model H_{nh} , and the GBZ is calculated from an OBC chain with $N = 60$.

The degrees of the variables in the polynomial equations $f(E, z) = 0, g(M, z) = 0, h(E, M) = 0$ give the number of Riemann sheets for that variable. For general cases of Eq. (1), we have four $z(E)$ sheets [11], two $E(z)$ sheets [61, 73], two $z(M)$ sheets, two $M(z)$ sheets, four $M(E)$ sheets and two $E(M)$ sheets, which are illustrated for the model H_{nh} in Fig. S1(a)-(f) respectively. The GBZ curve, \mathcal{C}_{GBZ} , is a 1D curve in (z, E) space defined by

$$\mathcal{C}_{\text{GBZ}} = \{(z, E) \text{ where } |z_2| = |z_3| \text{ for Eq. (4)}\}. \quad (\text{S5})$$

This is plotted in black in Fig. S1(a)-(f). The branch points of the Riemann surfaces are physically relevant. The method for solving for the branch points is described in Ref. [59, 68]. The z -plane, E -plane, and M -plane branch points are different sets and are plotted in green, blue, and red points respectively in Fig. S1(a)-(f). For general cases of our model in Eq. (1), we have:

- Four z -plane branch points: These are found by calculating the roots of the discriminant of $f(E, z) = 0$ with respect to E . They correspond to gap closing points [90] and affect the eigenvalue topology [51, 52] (see SM Sec. VIII).
- Eight E -plane branch points: These are found by calculating the roots of the discriminant of $f(E, z) = 0$ with respect to z . Some of these correspond to the end points of the OBC spectra [68].
- Four M -plane branch points: These are found by calculating the roots of the discriminant of $g(M, z) = 0$ with respect to z . We use these in our general edge-state invariant in Eq. (10).

There are cases where there are less than four $z(E)$ sheets for Eq. (1) such as the SSH model. However, adding a small perturbation of a model with random couplings in Eq. (1) to this model will lead to four $z(E)$ sheets.

III. BULK EIGENVECTOR DEGENERACY M_{deg} AND E_{deg} DERIVATION

In this section, we derive the equation for M_{deg} in Eq. (8). We can write Eq. (5) as

$$M = \frac{H_{ab}(z)}{E(z) - H_{aa}(z)} = \frac{E(z) - H_{bb}(z)}{H_{ba}(z)} \quad (\text{S6})$$

where H from Eq. (1) is written as

$$H = \begin{bmatrix} H_{aa} & H_{ab} \\ H_{ba} & H_{bb} \end{bmatrix}. \quad (\text{S7})$$

This leads to two equations:

$$z[(E - H_{aa})M - H_{ab}] = 0 \quad (\text{S8})$$

$$z[(H_{ba}M - (E - H_{bb})] = 0, \quad (\text{S9})$$

which give:

$$-Mt_{aa,-1} - t_{ab,-1} - Mt_{aa,0}z - t_{ab,0}z - Mt_{aa,1}z^2 - t_{ab,1}z^2 + MzE = 0, \quad (\text{S10})$$

$$Mt_{ba,-1} + t_{bb,-1} + Mt_{ba,0}z + t_{bb,0}z + Mt_{ba,1}z^2 + t_{bb,1}z^2 - zE = 0. \quad (\text{S11})$$

Up to this point, the equations are completely general and can be used to determine M for any pair of (z, E) on the band structure. Now we apply the edge state criterion that at a certain E , there are two different z solutions that shares the same M (see discussions around Eqs. (10) of the main text as well as SM Sec. V). This can also be interpreted as having two different z solutions at fixed E and M . Since Eq. (S10) and (S11) each has a set of two z solutions and the solution sets are required to be the same, the left hand side of Eqs. (S10) and (S11) must be proportional to each other. If we then collect the coefficients of z^2 and z^0 terms, the ratio of the z^2 coefficient over the z^0 coefficient for both equations must be the same, leading to Eq. (8):

$$\begin{aligned} & M_{\text{deg}}^2 (t_{aa,1}t_{ba,-1} - t_{aa,-1}t_{ba,1}) + (t_{ab,1}t_{bb,-1} - t_{ab,-1}t_{bb,1}) \\ & + M_{\text{deg}} (t_{ab,1}t_{ba,-1} - t_{ab,-1}t_{ba,1} + t_{aa,1}t_{bb,-1} - t_{aa,-1}t_{bb,1}) = 0. \end{aligned}$$

We note that the definition of M and the resulting M_{deg} are dependent on the basis for the Hamiltonian; a similarity transformation on $H(z)$ changes the values of M_{deg} but not the edge state energies E_{deg} . As such, we also present an analytical equation for E_{deg} , which can be derived by comparing the coefficients from z^2 and z^1 terms and substituting $M = M_{\text{deg}}$. The full expression for E_{deg} reads:

$$\begin{aligned} E_{\text{deg}} = & \left| \begin{array}{cc} \langle h_+, h_+ \rangle & \langle h_+, h_- \rangle \\ \langle h_-, h_+ \rangle & \langle h_-, h_- \rangle \end{array} \right|^{-1} \left(- \left| \begin{array}{ccc} d_{o+} & d_{o0} & d_{o-} \\ \langle h_+, h_+ \rangle & \langle h_+, h_0 \rangle & \langle h_+, h_- \rangle \\ \langle h_-, h_+ \rangle & \langle h_-, h_0 \rangle & \langle h_-, h_- \rangle \end{array} \right| \right. \\ & \left. \pm \sqrt{\left| \begin{array}{ccc} \langle h_+, h_+ \rangle & \langle h_+, h_0 \rangle & \langle h_+, h_- \rangle \\ \langle h_0, h_+ \rangle & \langle h_0, h_0 \rangle & \langle h_0, h_- \rangle \\ \langle h_-, h_+ \rangle & \langle h_-, h_0 \rangle & \langle h_-, h_- \rangle \end{array} \right| \left(\left| \begin{array}{cc} \langle h_+, h_+ \rangle & \langle h_+, h_- \rangle \\ \langle h_-, h_+ \rangle & \langle h_-, h_- \rangle \end{array} \right| - \langle d_{o+}h_- - d_{o-}h_+, d_{o+}h_- - d_{o-}h_+ \rangle \right)} \right). \quad (\text{S12}) \end{aligned}$$

where $d_{o+} = \text{tr } h_+/2$, $d_{o0} = \text{tr } h_0/2$, $d_{o-} = \text{tr } h_-/2$, and $\langle A, B \rangle \equiv \text{tr}[(A - \text{tr } A/2)(B - \text{tr } B/2)]/2$. As the dependence of E_{deg} on H is expressed entirely through traces instead of matrix elements, the invariance of E_{deg} with respect to similarity transformations have been established. For the nearest-neighbour model considered here, there are only two E_{deg} values for the entire band structure. For each E_{deg} , four z solutions can be solved from Eq. (4), corresponding to four M values. Two of these M values becomes degenerate and equals to M_{deg} . Similar to M_{deg} , the E_{deg} values can be calculated regardless of whether E_{deg} represents an actual edge state. For an E_{deg} that corresponds to an edge state, the distance of E_{deg} to the OBC spectrum provides a measure of the stability of the edge state. For an E_{deg} that does not correspond to an edge state, the distance of E_{deg} to the OBC spectrum provides a measure of how far the system is from the emergence of an edge state.

IV. NUMERICAL DETAILS FOR PHASE DIAGRAMS IN FIG. 3

A. Hermitian phase diagram

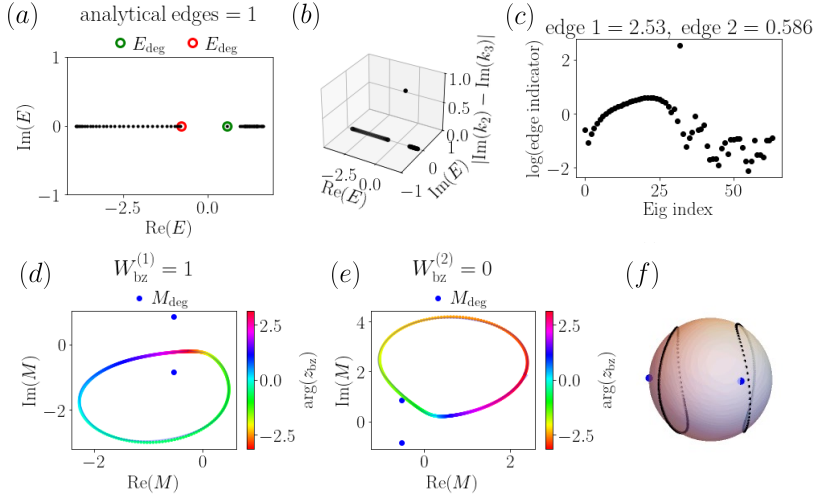


FIG. S2. (a) E_{obc} on complex E plane. E_{deg} is plotted as a green circle if it corresponds to an edge state and a red circle if it does not (with total number of analytical edge states in the title). (b) E_{obc} in $\{\text{Re}(E), \text{Im}(E), |\text{Im}(k_2) - \text{Im}(k_3)|\}$ space. (c) Logarithm of edge indicators of all E_{obc} modes, with top two in the title. (d,e) $M(\mathcal{C}_{\text{BZ}}^{(i)})$ colored by $\arg(z)$ on M -plane. Both M_{deg} points are in blue, and numerically calculated $W_{\text{BZ}}^{(i)}$ from Eq. (9) is in the title. Here $i = 1, 2$ is for (d) and (e) respectively. (f) $M(\mathcal{C}_{\text{BZ}})$ and M_{deg} on the M -Riemann sphere in black and blue respectively. All subplots are for the model H_{h} for $N = 32$.

In Fig. 3(a) we verify the Hermitian invariant Eq. (9) for the Hermitian model $H = (1 - \alpha)H_{\text{h}} + \alpha H_{\text{ssh}}$ (parameters in SM Sec. I) with $t_2 = 1$, $\alpha = 0$ to 0.90 and $t_1 = -1.5$ to 1.5. For both α and t_1 , 80 values are selected equidistantly in the range, resulting in 6400 models. An example of the procedure for obtaining the numerical phase diagram of the Hermitian model is shown in Fig. S2 for the model H_{h} .

We numerically solve the open boundary spectrum E_{obc} with $N = 32$ and plot it in Fig. S2(a). We also solve for E_{deg} using Eq. (S12). Using E_{deg} , we can apply an ‘‘analytical edge state condition’’ where we classify an E_{deg} point as an edge state if and only if $|M_1 - M_2| < \epsilon$ or $|M_3 - M_4| < \epsilon$ at that point for some small ϵ tolerance (here we choose $\epsilon = 0.001$). We plot the E_{deg} point as a green circle if it corresponds to an edge state, and a red circle otherwise in Fig. S2(a). The number of E_{deg} that are edge states can be counted and is listed in the title as the number of ‘‘analytical edge states’’ in Fig. S2(a). Calculating E_{deg} or the number of analytical edges is not strictly necessary for the phase diagram in Fig. 3(a). However, it is a useful verification of the numerically calculated topological invariant, since the edge state may be close to the bulk bands and hard to distinguish without the analytical edge state criterion.

In Fig. S2(b,c), we calculate the edge state indicators shown in Fig. 3(a). We show in Fig. S2(b) E_{obc} in $\{\text{Re}(E), \text{Im}(E), |\text{Im}(k_2) - \text{Im}(k_3)|\}$ space. The edge states appear higher on the $|\text{Im}(k_2) - \text{Im}(k_3)|$ scale than the bulk states. For every E_{obc} mode, the edge state indicator is calculated as the second-largest Euclidean distance of the E_{obc} mode in $\{\text{Re}(E), \text{Im}(E), |\text{Im}(k_2) - \text{Im}(k_3)|\}$ space to all other E_{obc} modes. The second largest distance is selected because the first largest distance may point to the other edge state instead of the bulk. As the indicator estimates the distance from the E_{obc} mode to the bulk, it should be smaller for bulk states and larger for edge states. The edge state indicators for all E_{obc} modes are shown in log scale in Fig. 3(c) and the largest two are shown in the title. This gives the edge 1 and 2 indicators in Fig. 3(a). Note that in Hermitian models, one can also use IPR as an indicator for edge states.

In Fig. S2(d,e), we numerically calculate the Hermitian topological invariant in Eq. (9). There are two energy bands in the gapped case, and their image on the M -plane is $M(\mathcal{C}_{\text{BZ}}^{(1)})$ and $M(\mathcal{C}_{\text{BZ}}^{(2)})$. Since the GBZ reduces to the BZ, we use $z \in e^{i\theta}$ for 500 equally spaced values of $\theta \in [-\pi, \pi]$. We substitute these 500 z values into $E_{\pm}(z) = d_o(z) \pm \sqrt{d_x(z)^2 + d_y(z)^2 + d_z(z)^2}$, where the \pm sign distinguishes the two bands. With the (z, E) pairs, we use Eq. (5) to get $M(\mathcal{C}_{\text{BZ}}^{(1)})$ and $M(\mathcal{C}_{\text{BZ}}^{(2)})$. We plot $M(\mathcal{C}_{\text{BZ}}^{(1)})$ and $M(\mathcal{C}_{\text{BZ}}^{(2)})$ separately in Fig. S2(d) and (e) respectively. We fit a function to $M(\mathcal{C}_{\text{BZ}}^{(1)})$ and $M(\mathcal{C}_{\text{BZ}}^{(2)})$, which we use to numerically count the number of M_{deg} points inside $M(\mathcal{C}_{\text{BZ}}^{(i)})$. We plot both M_{deg} points (calculated from Eq. (8) or using E_{deg}) in Fig. S2(d) and (e). $W_{\text{BZ}}^{(i)}$ is numerically found by

counting the number of M_{deg} points inside $M(\mathcal{C}_{\text{GBZ}}^{(i)})$ and taking mod 2. The direction of winding is removed by the mod 2 and a parity count is sufficient.

In Fig. S2(f) we plot $M(\mathcal{C}_{\text{GBZ}})$ and M_{deg} on the M -Riemann sphere in black and blue respectively.

B. Non-Hermitian phase diagram

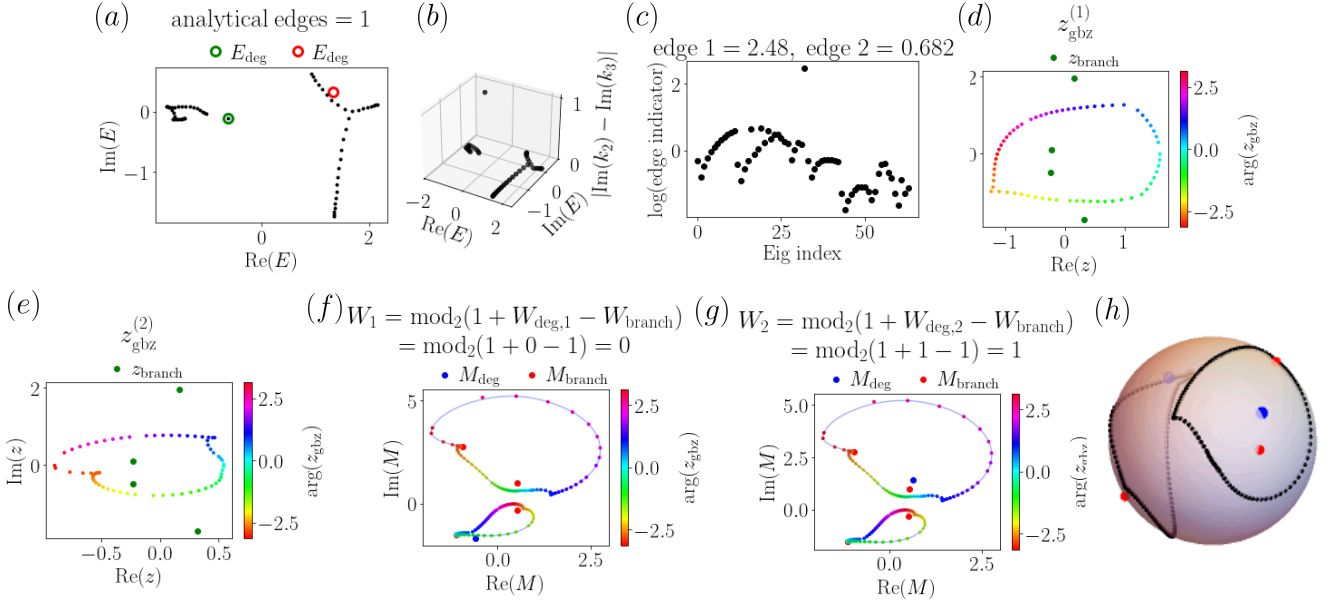


FIG. S3. (a) E_{obc} on complex E plane. E_{deg} is plotted as a green if it corresponds to an edge and a red circle if it does not (with total number of analytical edge states in the title). (b) E_{obc} in $\{\text{Re}(E), \text{Im}(E), |\text{Im}(k_2) - \text{Im}(k_3)|\}$ space. (c) Logarithm of edge indicators of all E_{obc} modes, with top two in the title. (d,e) z from $\mathcal{C}_{\text{GBZ}}^{(i)}$ is plotted on complex z -plane colored by $\arg(z)$. z_{branch} is plotted in green. (f,g) $M(\mathcal{C}_{\text{GBZ}})$ colored by $\arg(z)$ on M -plane. M_{branch} is plotted in red. We plot $M_{\text{deg},j}$ and numerical calculation of W_j from Eq. (10) is given in the title for $j = 1, 2$ in (f) and (g) respectively. (h) $M(\mathcal{C}_{\text{GBZ}})$, M_{deg} and M_{branch} on the M -Riemann sphere in black, blue and red respectively. All subplots are for the model H_{nh} for $N = 32$.

In Fig. 3(b) we verify the general invariant Eq. (10) for the non-Hermitian model $H = (1 - \alpha)H_{\text{nh}} + \alpha H_{\text{ssh}}$ (parameters in SM Sec. I) with $t_2 = 1$, $\alpha = 0$ to 0.90 and $t_1 = -1.5$ to 1.5. For both α and t_1 , 80 values are selected equidistantly in the range, resulting in 6400 models. An example of the procedure for obtaining the numerical phase diagram of the non-Hermitian model is shown in Fig. S3 for the model H_{nh} .

The calculation for E_{obc} , E_{deg} and the edge state indicators are the same for the non-Hermitian case as for the Hermitian case described in SM Sec. IV A and is depicted in Fig. S3(a-c) for the non-Hermitian model.

In Fig. S3(d-g), we show the steps to calculate the general invariant in Eq. (10) for our non-Hermitian model. Unlike the Hermitian model, we must numerically calculate the GBZ. Different methods are described in Ref. [59]. For non-Hermitian models, the GBZ may braid, and the braiding topology (if it is a braid) can be determined by the number of z_{branch} points enclosed by the GBZ on the z -plane [68] (see SM Sec. VIII). The different braiding topology determines whether $M(\mathcal{C}_{\text{GBZ}})$ consists of distinct loops in the M -plane, which affects fitting a function (or multiple functions) to $M(\mathcal{C}_{\text{GBZ}})$. For the phase diagram in Fig. 3(b), we observed that there were two z_{branch} points enclosed by the GBZ on the z -plane for nearly the entire phase diagram. While there does appear to be a braiding transition within the parameter space of Fig. 3(b), this transition happens over a very small parameter range in comparison to the grid size of the t_1 and α values, so we can reasonably approximate the non-Hermitian model as being in an unlinked GBZ phase (see SM Sec. VIII) across the models evaluated in Fig. 3(b). After knowing the braiding topology of the GBZ, we can sort the calculated GBZ into subGBZ [51, 61, 90] loops. Here, the two links of the unlink are the subGBZ loops. An analytical method to sort the subGBZ loops is described in Ref. [51], and other clustering algorithms based on machine learning [91–95] are also available. In Fig. S3(d-e) we plot the two subGBZ loops on the z plane to check that they have been sorted properly.

By sorting the subGBZ loops each by $\arg(z)$, we fit a function to the distinct $M(\mathcal{C}_{\text{GBZ}}^{(i)})$ loops by sorting $M(\mathcal{C}_{\text{GBZ}}^{(i)})$ by its respective $\arg(z)$ value from the GBZ. In Fig. S3(f,g) we plot *both* $M(\mathcal{C}_{\text{GBZ}}^{(1)})$ and $M(\mathcal{C}_{\text{GBZ}}^{(2)})$ loops but plot $M_{\text{deg},1}$

and $M_{\text{deg},2}$ points *separately* for Fig. S3(f) and Fig. S3(g) respectively. Note that this contrasts to the process in the Hermitian case in SM Sec. IV A and is a consequence of the way Eq. (9) and Eq. (10) is constructed. M_{branch} is plotted in red in Fig. S3(f,g). Using the information in Fig. S3(f) and (g) one can calculate W_1 and W_2 respectively from Eq. (10). The calculation requires finding the winding number of $M_{\text{deg},j}$ (which is $W_{\text{deg},j}$) and the winding number of any one of the four M_{branch} points (which is W_{branch}). We again calculated the winding numbers by using a count of $M_{\text{deg},j}$ or M_{branch} in the fitted $M(\mathcal{C}_{\text{GBZ}})$ loops and these counts are listed in the second line of the title of Fig. S3(f,g). For non-Hermitian models, one must in addition check whether there are intersecting $M(\mathcal{C}_{\text{GBZ}})$ loops when numerically counting the winding numbers.

In Fig. S2(f) we plot $M(\mathcal{C}_{\text{GBZ}})$, M_{deg} , M_{branch} on the M -Riemann sphere in black, blue and red respectively.

C. Discussion on the phase diagrams

We note that in these processes, the E_{deg} or M_{deg} values must be evaluated to calculate the topological invariant in Eq. (9) and Eq. (10). However, from E_{deg} or M_{deg} , one could have already found the number of edge states by applying the analytical edge state criteria. Thus, Eq. (9) and Eq. (10) does not provide a more efficient computational technique to calculate edge states – it takes more steps than the analytical edge state condition. The significance of Eq. (9) and Eq. (10) is that it quantifies the topological stability or robustness of the edge or non-edge states calculated from E_{deg} .

We also give an animation of the plots in Fig. S2 for a slice of the Hermitian phase diagram along $t_1 = 1.5$ verifying Eq. (9) in Fig. 3(a) and an animation of the plots in Fig. S3 for the a slice of the non-Hermitian phase diagram along $t_1 = -1.01$ verifying Eq. (10) in Fig. 3(b) in Supplementary Gifs 1 and 2 respectively. In these animations, we also include a visualization of all eigenvectors at each point in the phase diagram.

V. ANALYTICAL EDGE STATE CRITERIA

Here we provide a more detailed discussion of the conditions for edge states. The bulk model Eq. (1) without boundary conditions admit plane-wave-like states as solutions at a specific energy E . The states can be written as $C_j(\alpha_j, \beta_j)^T z_j^n$, where $j = 1, 2, 3, 4$, C_j are complex constants, z_j are the solutions from $\det(H(z) - E\mathbb{1}) = 0$, n denotes the unit cell index, and $(\alpha_j, \beta_j)^T$ are eigenvectors of $H(z_j)$ at eigenvalue E . In the presence of a boundary, a general mode solution is a superposition of all the possible states:

$$\psi_n = C_1 \begin{pmatrix} \alpha_1 \\ \beta_1 \end{pmatrix} z_1^n + C_2 \begin{pmatrix} \alpha_2 \\ \beta_2 \end{pmatrix} z_2^n + C_3 \begin{pmatrix} \alpha_3 \\ \beta_3 \end{pmatrix} z_3^n + C_4 \begin{pmatrix} \alpha_4 \\ \beta_4 \end{pmatrix} z_4^n \quad (\text{S13})$$

We now impose open-boundary conditions (OBC) by requiring that $\psi_0 = 0$ and $\psi_N = 0$. For Eq. (S13) to have nonzero solutions, the determinant of the coefficient matrix must be zero [67]:

$$\begin{vmatrix} \alpha_1 & \alpha_2 & \alpha_3 & \alpha_4 \\ \beta_1 & \beta_2 & \beta_3 & \beta_4 \\ \alpha_1 z_1^N & \alpha_2 z_2^N & \alpha_3 z_3^N & \alpha_4 z_4^N \\ \beta_1 z_1^N & \beta_2 z_2^N & \beta_3 z_3^N & \beta_4 z_4^N \end{vmatrix} = 0. \quad (\text{S14})$$

We expand the determinant and order the terms by z magnitudes:

$$\begin{vmatrix} \alpha_1 & \alpha_2 \\ \beta_1 & \beta_2 \end{vmatrix} \begin{vmatrix} \alpha_3 & \alpha_4 \\ \beta_3 & \beta_4 \end{vmatrix} z_3^N z_4^N - \begin{vmatrix} \alpha_1 & \alpha_3 \\ \beta_1 & \beta_3 \end{vmatrix} \begin{vmatrix} \alpha_2 & \alpha_4 \\ \beta_2 & \beta_4 \end{vmatrix} z_2^N z_4^N + \dots = 0 \quad (\text{S15})$$

and using $M_i = \alpha_i/\beta_i$, we get

$$\begin{vmatrix} M_1 & M_2 \\ 1 & 1 \end{vmatrix} \begin{vmatrix} M_3 & M_4 \\ 1 & 1 \end{vmatrix} - \begin{vmatrix} M_1 & M_3 \\ 1 & 1 \end{vmatrix} \begin{vmatrix} M_2 & M_4 \\ 1 & 1 \end{vmatrix} \left(\frac{z_2}{z_3}\right)^N + \dots = 0. \quad (\text{S16})$$

For Eq. (S16) to hold, the two leading terms should cancel in the $N \rightarrow \infty$ limit. The first way requires $|z_2|/|z_3| \rightarrow 1$ and is the condition for the GBZ. The second way requires $(M_1 - M_2)(M_3 - M_4) \rightarrow 0$ and leads to either $M_1 = M_2$ or $M_3 = M_4$ (the edge states).

VI. PROOF OF THE GENERAL EDGE-STATE INVARIANT

The proof consists of several components. In SM Sec. [VIA](#) we show that, under general conditions, the band structure defines a Riemann surface that is topologically equivalent to a torus. This torus can be represented by the Weierstrass elliptic function $\wp(\tau; g_2, g_3)$, where τ is the ‘‘torus parameter’’ and the elliptic invariants g_2 and g_3 can be obtained from the coupling coefficients. Then in SM Sec. [VIB](#) we formulate the edge state condition as a winding integral on the τ plane. With a change of variables from τ to M , the integration can be interpreted as a winding number on the M plane. In SM Sec. [VIC](#) we show the additional property that the two edge states cannot share the same side of the chain, which is not necessary for the proof but can be applied to specific cases.

A. Riemann surface for the band structure

We begin with the band structure $\det(H - E\mathbb{I}) = 0$, which can be expanded as

$$E^2 - E \operatorname{tr} H + \det H = 0 \quad (\text{S17})$$

The discriminant of the band structure with respect to E , denoted as Δ , can be found as

$$\Delta = (\operatorname{tr} H)^2 - 4 \det H = -\det(2H - \operatorname{tr} H) \quad (\text{S18})$$

and the band structure can be rearranged as

$$z^2 \left(E - \frac{\operatorname{tr} H}{2} \right)^2 = \frac{z^2 \Delta}{4} \quad (\text{S19})$$

Under the assumptions that H only contains nearest-unit-cell couplings, each entry of H is a Laurent polynomial in z with powers of z from -1 to 1 , and $z^2 \Delta$ is a polynomial in z with a degree at most four. The fundamental theorem of algebra implies that $z^2 \Delta = 0$ then has four solutions (if the degree of $z^2 \Delta$ is less than four, we include $z = \infty$ in the solution list).

The band structure, after multiplication by z^2 , is a polynomial in z and E , and therefore is an algebraic curve. An algebraic curve is also a compact Riemann surface if the curve is smooth. For the band structure, the smoothness condition is that there are no duplicate roots in $z^2 \Delta = 0$ (including $z = \infty$). This is readily satisfied by models with general coefficients. We will assume that $z^2 \Delta = 0$ does not contain duplicate roots from here on. In such cases, Eq. (S19) represents an elliptic curve of genus 1 and its Riemann surface is topologically equivalent to a torus [96].

We now write $\Delta = \delta_{-2} z^{-2} + \delta_{-1} z^{-1} + \delta_0 + \delta_1 z + \delta_2 z^2$, where the δ 's are complex numbers determined from H . We also denote one of the roots of $z^2 \Delta = 0$ as z_Δ and define the following quantities:

$$g_2 = 16\delta_{-2}\delta_2 - 4\delta_{-1}\delta_1 + \frac{4}{3}\delta_0^2, \quad (\text{S20})$$

$$g_3 = -4\delta_{-2}\delta_1^2 - 4\delta_{-1}^2\delta_2 + \frac{32}{3}\delta_{-2}\delta_0\delta_2 + \frac{4}{3}\delta_{-1}\delta_0\delta_1 - \frac{8}{27}\delta_0^3, \quad (\text{S21})$$

$$p_1 = \delta_{-1} + 2\delta_0 z_\Delta + 3\delta_1 z_\Delta^2 + 4\delta_2 z_\Delta^3, \quad (\text{S22})$$

$$p_2 = \frac{1}{3}(\delta_0 + 3\delta_1 z_\Delta + 6\delta_2 z_\Delta^2). \quad (\text{S23})$$

Then the following parametrization expresses z and E in terms of the Weierstrass elliptic function $\wp(\tau; g_2, g_3)$:

$$z = z_\Delta + \frac{p_1}{\wp(\tau; g_2, g_3) - p_2} \quad (\text{S24})$$

$$E = \frac{\operatorname{tr} H}{2} + \frac{\wp'(\tau; g_2, g_3)}{4z} \frac{p_1}{[\wp(\tau; g_2, g_3) - p_2]^2} \quad (\text{S25})$$

where $\wp(\tau; g_2, g_3)$ satisfies the differential equation $\wp'^2 = 4\wp^3 - g_2\wp - g_3$ and the prime indicates derivative with respect to τ .

The Weierstrass elliptic function is doubly periodic in the complex τ plane, i.e. $\wp(\tau + \omega_1; g_2, g_3) = \wp(\tau + \omega_2; g_2, g_3) = \wp(\tau; g_2, g_3)$, where the periods ω_1 and ω_2 are linearly-independent complex numbers as functions of g_2 and g_3 . As such, τ , $\tau + \omega_1$, and $\tau + \omega_2$ all represent the same (z, E) point on the Riemann surface. It is sufficient to consider the range of τ within the fundamental parallelogram bounded by 0 , ω_1 , $\omega_1 + \omega_2$, and ω_2 on the τ plane (see Fig. S4 for an example), where each (z, E) has a one-to-one correspondence with τ . In addition, opposite edges of this parallelogram should be “glued together” (i.e., identified) due to periodicity. This shows that the Riemann surface, parametrized by τ , is topologically equivalent to a torus.

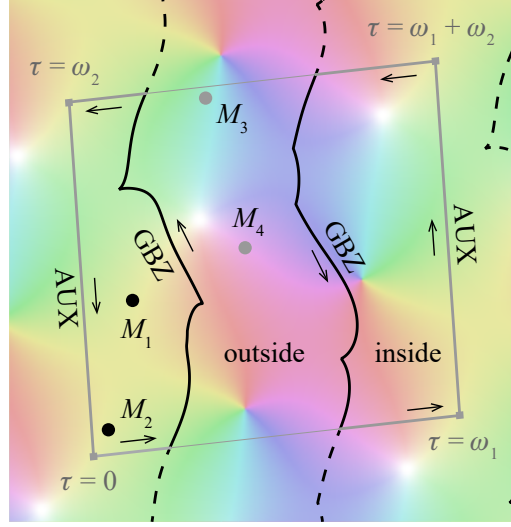


FIG. S4. The complex M as a function of the “torus parameter” τ . Here the Hamiltonian is given by H_{nh} (Sec. I and Fig. S3). The τ plane is colored by M values where the color gives $\arg(M)$ and the brightness gives $|M|$. The fundamental parallelogram (gray) is bounded by $\tau = 0$, $\tau = \omega_1$, $\tau = \omega_1 + \omega_2$, and $\tau = \omega_2$. The set of M values for the only edge state in the model, where $M_1 = M_2$, have been marked on the plane as dots. The GBZ (black curves) extends infinitely on the τ plane, but only the sections inside the fundamental parallelogram (solid) are being considered here. The GBZ divides the fundamental parallelogram into an outside and an inside. The integration contour consists of the GBZ itself as well as auxiliary contours along the parallelogram (thick gray lines). The contour direction (arrows) is chosen such that it circles around the GBZ inside in the counterclockwise direction.

B. Number of edge states as a contour integration

In Section V we have proved that the existence of edge states requires $M_1 = M_2$ or $M_3 = M_4$. Before formulating this condition as an integral on the GBZ, we require some properties of the mapping from the Riemann surface of the band structure to M , which we discuss in the following.

We first show that there are exactly two zeros of $M(z, E) - M_{\text{deg}}$ on the torus, counted with multiplicity. This can be seen from Eqs. (S10) and (S11), where eliminating E leads to a quadratic equation of z . In fact, this conclusion is independent of the edge state criterion, and the M_{deg} can be replaced with any complex number. An arbitrary value of M has two preimages on the torus if M is not a branch point. If M is a branch point, the preimage is a single point on the torus but the zero of $M - M_{\text{branch}}$ has multiplicity two.

Now we introduce the notion of the inside and outside of the GBZ on the band structure Riemann surface. We define a point (z, E) to be inside the GBZ if z is among the two roots with the smallest amplitudes ($z = z_1$ or $z = z_2$, where z_1 to z_4 are the four solutions sorted in non-decreasing amplitude of the band structure equation at E). By the continuity of polynomial roots, all points inside the GBZ form (possibly disconnected) regions and are separated from the outside of the GBZ by the GBZ $|z_2| = |z_3|$. The edge state criterion can then be stated as whether the preimages of a single M_{deg} are both inside or both outside the GBZ on the Riemann surface. If both preimages are inside the GBZ, then $M_{\text{deg}} = M_1 = M_2$ and corresponds to an edge state. Similarly, if both preimages are outside the GBZ, then $M_{\text{deg}} = M_3 = M_4$ and also corresponds to an edge state. If one preimages is inside the GBZ and the other is outside the GBZ, then M_{deg} does not correspond to an edge state. The number of preimages inside the GBZ

for M_{deg} can also be viewed as the number of times the region containing M_{deg} is covered by the mapping from the inside of the GBZ to the M -Riemann sphere.

We can now assign a contour direction to each piece of the GBZ on the torus (Fig. S4), where the inside of the GBZ on the τ plane appears on the left when moving in the positive direction of the contour. We also add auxiliary contours on the boundaries of the fundamental parallelogram (denoted as AUX) so that the inside of the GBZ is completely enclosed in the contour. We can then define the winding integral of $M - M_{\text{deg},1}$ along the boundary of the inside of the GBZ:

$$w_{\text{deg},1} = \frac{1}{2\pi i} \oint_{\text{GBZ} + \text{AUX}} d\tau \frac{d}{d\tau} \ln(M(\tau) - M_{\text{deg},1}) \quad (\text{S26})$$

The subscript 1 indicates that only one of the M_{deg} is currently being considered. By the argument principle, this integral will count the number of zeros minus the number of poles of $M - M_{\text{deg},1}$ inside the GBZ. We note that the pole of $M - M_{\text{deg},1}$ is simply the pole of M . To remove this quantity, we consider the winding integral of $M - M_{\text{branch}}$, where M_{branch} is any one of the four branch points on the M sphere:

$$w_{\text{branch}} = \frac{1}{2\pi i} \oint_{\text{GBZ} + \text{AUX}} d\tau \frac{d}{d\tau} \ln(M(\tau) - M_{\text{branch}}) \quad (\text{S27})$$

The difference of these two winding numbers give the difference of the number of zeros for $M - M_{\text{deg},1}$ and $M - M_{\text{branch}}$. The numbers of zeros for $M - M_{\text{deg}}$ is even if $M_{\text{deg},1}$ leads to an edge state, and odd if not an edge state. On the other hand, the number of zeros of $M - M_{\text{branch}}$ is always an even number due to the degeneracy. Therefore, we can define

$$w_1 = w_{\text{deg},1} - w_{\text{branch}} = \frac{1}{2\pi i} \oint_{\text{GBZ} + \text{AUX}} d\tau \frac{d}{d\tau} \ln \frac{M(\tau) - M_{\text{deg},1}}{M(\tau) - M_{\text{branch}}} \text{ mod } 2 \quad (\text{S28})$$

The mod 2 operation effectively removes the contributions from zeros of $M - M_{\text{branch}}$. As such, $w_1 = 0$ indicates an edge state from $M_{\text{deg},1}$, while $w_1 = 1$ indicates no edge states from $M_{\text{deg},1}$. Another difference $w_2 = w_{\text{deg},2} - w_{\text{branch}}$ can be defined for $M_{\text{deg},2}$.

Finally, we note that the integrations on the auxiliary contours will cancel each other due to the periodicity of τ , leading to

$$w_1 = \frac{1}{2\pi i} \oint_{\text{GBZ}} d\tau \frac{d}{d\tau} \ln \frac{M(\tau) - M_{\text{deg},1}}{M(\tau) - M_{\text{branch}}} \text{ mod } 2 \quad (\text{S29})$$

A change of variables from τ to M then converts the integral to the M plane:

$$w_1 = \frac{1}{2\pi i} \oint_{M(\text{C}_{\text{GBZ}})} dM \frac{d}{dM} \ln \frac{M - M_{\text{deg},1}}{M - M_{\text{branch}}} \text{ mod } 2 \quad (\text{S30})$$

We also note that reversing the orientation of any loop will change the winding numbers by an even number, so the orientation of GBZ is not required as long as the integration paths forms loops along the GBZ:

$$w_1 = \frac{1}{2\pi i} \int_{M(\text{C}_{\text{GBZ}})} dM \frac{d}{dM} \ln \frac{M - M_{\text{deg},1}}{M - M_{\text{branch}}} \text{ mod } 2 \quad (\text{S31})$$

An even w_1 indicates an edge state. Adding the parity flip by defining $W_1 = w_1 + 1 \text{ mod } 2$ reproduces Eq. (10) and completes the proof.

C. Distributions of the edge states

In this subsection we prove that the two edge states cannot be all on the left edge or all on the right edge. While this knowledge is not necessary for the proof of the winding numbers, it can be used to further simplify the integral in some special cases such as in Hermitian models. The idea is that the states participating in edge state formations cannot all have small $|z|$ amplitudes and therefore must belong to different edges.

Denote z_{A1} and z_{A2} as the solutions to Eqs. (S10) and (S11) when $M = M_{\text{deg},1}$, and z_{B1} and z_{B2} when $M = M_{\text{deg},2}$. Applying Vieta's formula to Eq. (S10) leads to

$$|z_{A1}z_{A2}| = \left| \frac{M_{\text{deg},1}t_{aa,-1} + t_{ab,-1}}{M_{\text{deg},1}t_{aa,1} + t_{ab,1}} \right| \quad (\text{S32})$$

$$|z_{B1}z_{B2}| = \left| \frac{M_{\text{deg},2}t_{aa,-1} + t_{ab,-1}}{M_{\text{deg},2}t_{aa,1} + t_{ab,1}} \right| \quad (\text{S33})$$

These can be multiplied together and results in

$$|z_{A1}z_{A2}z_{B1}z_{B2}| = \left| \frac{t_{aa,-1}^2 M_{\text{deg},1} M_{\text{deg},2} + t_{aa,-1} t_{ab,-1} (M_{\text{deg},1} + M_{\text{deg},2}) + t_{ab,-1}^2}{t_{aa,1}^2 M_{\text{deg},1} M_{\text{deg},2} + t_{aa,1} t_{ab,1} (M_{\text{deg},1} + M_{\text{deg},2}) + t_{ab,1}^2} \right| \quad (\text{S34})$$

The values of the symmetric polynomials $M_{\text{deg},1}M_{\text{deg},2}$ and $M_{\text{deg},1} + M_{\text{deg},2}$ can be obtained by applying Vieta's formula to Eq. (8). After some rearrangements we get

$$|z_{A1}z_{A2}z_{B1}z_{B2}| = \left| \frac{t_{aa,-1}t_{bb,-1} - t_{ab,-1}t_{ba,-1}}{t_{aa,1}t_{bb,1} - t_{ab,1}t_{ba,1}} \right| = \left| \frac{\det h_-}{\det h_+} \right| \quad (\text{S35})$$

On the other hand, we can expand the band structure $E^2 - E \text{tr} H + \det H = 0$, which results in

$$z^{-2} \det h_- + \dots + z^2 \det h_+ = 0 \quad (\text{S36})$$

where the z^{-1} , z^0 and z^1 terms are not relevant to the current analysis and are therefore omitted. At any E , application of the Vieta's formula to the band structure leads to

$$|z_1 z_2 z_3 z_4| = \left| \frac{\det h_-}{\det h_+} \right| \quad (\text{S37})$$

Now assume that both edges states are on the left edge, i.e. z_{A1} and z_{A2} are the two solutions with the smallest magnitude among the four z solutions of $E_{\text{deg},1}$ and the same holds for $E_{\text{deg},2}$. This would imply that

$$|z_{A1}z_{A2}| < \left| \frac{\det h_-}{\det h_+} \right|^{1/2} \quad (\text{S38})$$

$$|z_{B1}z_{B2}| < \left| \frac{\det h_-}{\det h_+} \right|^{1/2} \quad (\text{S39})$$

These can be multiplied together and results in

$$|z_{A1}z_{A2}z_{B1}z_{B2}| < \left| \frac{\det h_-}{\det h_+} \right| \quad (\text{S40})$$

which is in direct contradiction to Eq. (S35). We therefore conclude that if there are two edge states in the same system, one must be on the left edge and the other one must be on the right edge.

VII. PROOF OF THE HERMITIAN EDGE-STATE INVARIANT

In this case we consider the special case of Hermitian models. We show that under a quasi-chiral basis as defined below, the eigenmodes from one band will always be concentrated on one of the lattice sites. Together with the orthogonality of modes (inversion symmetry of M) between the two bands, this implies that the two $M(\mathcal{C}_{\text{BZ}})$ loops are simple loops on the M -Riemann sphere. We also use the fact that if there exists two edge states, they can not originate from the same side of the chain (SM Sec. VIC). These results can be combined to remove the M_{branch} correction from the general winding number and lead to integrations over each band that more closely resemble the invariants of the Berry-Zak phase as applicable to models with symmetries.

For later convenience we rewrite the Hamiltonian as

$$H = \frac{\text{Tr} H}{2} \mathbb{I} + (\mathbf{v}_0 + \mathbf{v}_{\text{sym}} \cos k + \mathbf{v}_{\text{asym}} \sin k) \cdot \boldsymbol{\sigma}^* \quad (\text{S41})$$

where $\mathbf{v}_0 = \text{Tr}(h_0 \boldsymbol{\sigma}^*)/2$, $\mathbf{v}_{\text{sym}} = \text{Tr}[(h_+ + h_-) \boldsymbol{\sigma}^*]/2$ and $\mathbf{v}_{\text{asym}} = i \text{Tr}[(h_+ - h_-) \boldsymbol{\sigma}^*]/2$ are three real 3D vectors and $\boldsymbol{\sigma} = (\sigma_x, \sigma_y, \sigma_z)$ are the vector of Pauli matrices. The conjugation for $\boldsymbol{\sigma}$ replaces σ_y to $-\sigma_y$ and aligns the Bloch sphere coordinates with the M Riemann sphere defined here. Applying unitary transformations to H is equivalent to

simultaneously applying the same rotation to \mathbf{v}_0 , \mathbf{v}_{sym} and \mathbf{v}_{asym} . As such, we can choose a basis where both \mathbf{v}_{sym} and \mathbf{v}_{asym} have no Z components. This is achieved by setting the Z direction perpendicular to the plane formed by \mathbf{v}_{sym} and \mathbf{v}_{asym} . We term this basis a quasi-chiral basis.

Using Eq. (7), the location of eigenvectors on the M Riemann sphere is given by the direction of $\pm(\mathbf{v}_0 + \mathbf{v}_{\text{sym}} \cos k + \mathbf{v}_{\text{asym}} \sin k)$. Under the quasi-chiral basis, the Z component of each band is $\mathbf{v}_{0,Z}$ and is a constant. For $\mathbf{v}_{0,Z} \neq 0$, one band is restricted to the southern hemisphere and the other band is restricted to the northern hemisphere. In addition, since the vector $\mathbf{v}_0 + \mathbf{v}_{\text{sym}} \cos k + \mathbf{v}_{\text{asym}} \sin k$ represents an ellipse in the 3D space, its Bloch sphere projection will divide the sphere into at most two regions (division does not occur if the projected ellipse degenerates into a backtracking curve). Using the correspondence between the Bloch sphere and the M -Riemann sphere, both $M(\mathcal{C}_{\text{BZ}})$ loops do not cross the $|M| = 1$ circle and divides the M -Riemann sphere into at most three regions [Fig. S5(a)]: the region having the $M(\mathcal{C}_{\text{BZ}})$ loop with $|M| < 1$ as its boundary (designated as Region I), the region containing $|M| = 1$ (Region II), and the region having the $M(\mathcal{C}_{\text{BZ}})$ loop with $|M| > 1$ as its boundary (Region III). For $\mathbf{v}_{0,Z} = 0$, the $M(\mathcal{C}_{\text{BZ}})$ is restricted to the $|M| = 1$ circle, and divides the M -Riemann sphere into a single Region II or two regions (I and III), depending on whether the loop circles around the origin. We note that the two $M(\mathcal{C}_{\text{BZ}})$ are central symmetric with respect to the Riemann sphere center due to the orthogonal relation between the eigenstates at each wavevector.

The Hermiticity of the model imposes the constraints $h_0 = h_0^\dagger$ and $h_+ = h_-^\dagger$ on the coupling coefficients. By comparing the eigenstates of H and H^\dagger at complex z values, $-1/M^*$ and $1/z^*$ are solutions to Eqs. (S10) and (S11) if M and z are solutions. As the BZ is simply the unit circle $|z| = 1$, the number of zeros for $M - M_{\text{deg}}$ inside the BZ equals the number of zeros for $M + 1/M_{\text{deg}}^*$ outside the BZ. In addition, the number of zeros inside the BZ remains the same for each M_{deg} inside the same region. If M_{deg} belongs to Region II, then $-1/M_{\text{deg}}^*$ also belongs to Region II, and as such has exactly a single zero inside the BZ. Similarly, the number of zeros inside the BZ for regions I and III adds up to two. Since they are across the $M(\mathcal{C}_{\text{BZ}})$ loop from Region II, they cannot each have a single zero in the BZ. As such, either Region I has no zeros inside the BZ and Region III has two, or vice versa.

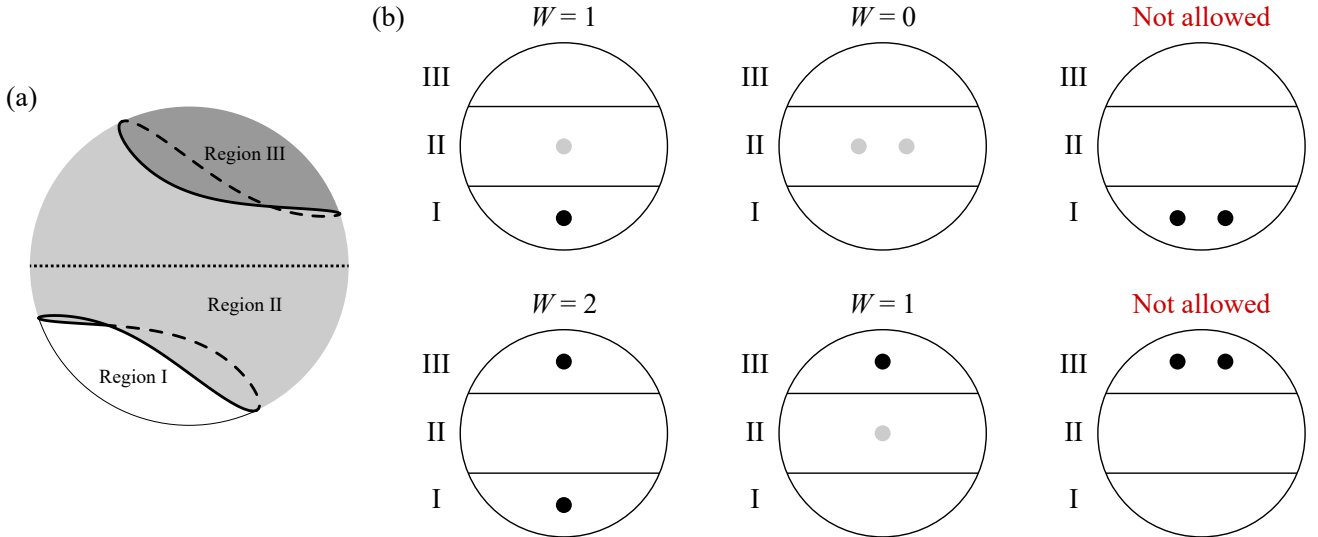


FIG. S5. The M Riemann sphere in the quasi-chiral basis and the combinatorial argument for the Hermitian invariant. (a) The M Riemann sphere for the Hamiltonian H_h (SM Sec. I and Fig. S2). The viewing direction is the same as Fig. 2(b) and is already in a quasi-chiral basis with Z pointing up and X pointing right. The two $M(\mathcal{C}_{\text{BZ}})$ loops (black curves) are separated by the equator ($|M| = 1$, dotted) and divides the sphere into Regions I, II and III. Region II indicates a single zero inside the BZ (light gray) and Region III indicates two zeros (dark gray). (b) All possible M_{deg} (dots) locations in the three regions on the M Riemann sphere. Black dots indicate the M_{deg} points are edge states, and gray dots indicate the M_{deg} points are not states. For the first four configurations, the results of Eq. (9) and Eq. (10) agree, while the last two configurations are not allowed (SM Sec. VIC).

At this point, the proof becomes a combinatorial problem of listing all the assignments of $M_{\text{deg},1}$ and $M_{\text{deg},2}$ to the three regions [Fig. S5(b)]. A M_{deg} point in regions I or III indicates an edge state due to the even number of zeros inside the BZ, while a M_{deg} in Region II is not an edge state. In addition, the configurations where the two points are both in Region I or Region III are not allowed, as this would indicate two edge states on the same edge. This leaves four possibilities: the points may be in Regions I and II, I and III, II and II, or II and III. In each case the Hermitian

integral agrees with the general integral, and its validity can thus be established in the quasi-chiral basis.

Finally, we note that Eq. (9) is invariant under Möbius transformations of M . As the unitary transformation performs rotations on the M -Riemann sphere, which is a subset of the Möbius transformations, the integral remains valid and is independent of the basis.

This proof does not generalize to non-Hermitian systems because the $M(\mathcal{C}_{\text{GBZ}})$ loops may intersect with each other on the M sphere and create more than three regions; see SM Sec. VIII C for an example.

VIII. EIGENVALUE TOPOLOGY OF THE GBZ

In the main text, we have argued that the emergence of edge states does not coincide with the gap closing conditions in general non-Hermitian models. Here we elaborate on the possible generalizations of gap closing conditions to non-Hermitian models and its connections to the eigenvalue topology of the GBZ.

A. Gap closing condition

While the term “gap” is unambiguous in Hermitian models, it can be interpreted in many ways in the non-Hermitian literature [13, 14, 16, 56, 90, 97]. Compared to Hermitian gaps between the distinct bands in the $\{\text{Re}(E), \text{Re}(k)\}$ space, non-Hermitian systems exhibit both point gaps (linked to skin effects) and line gaps (traditionally associated with edge states) [13, 14, 16, 97], and can be combined with two different types of spectra associated with periodic and open boundary conditions. For example, OBC bands coalescing at z -plane branch points [90] may close a line gap for OBC spectra drawn between the branch points. The GBZ invariants defined for non-Hermitian models with sublattice symmetry [8, 9] have edge-state transitions when the OBC spectrum coalesces the high-symmetry point (usually taken as $E = 0$).

In view of the above, we avoid a precise definition of gaps for non-Hermitian models. Instead, we make the following observations to justify the argument that the existence of edge states is independent of gap closing. Two non-Hermitian models may share the same continuous parts of PBC and OBC spectra as well as the GBZ, and one can be continuously deformed into the other while preserving the spectra. However, the existence of edge states and their locations can be different. This can be seen by counting the degrees of freedom (DOFs) involved in the model. The model in Eq. (1) has 12 complex DOFs given by the coupling coefficients. Similarity transformations of Eq. (1) (Möbius transformations of M) do not change the spectrum or the edge states and remove 3 DOFs. This leaves 9 DOFs and can be taken as the invariant quantities appearing in Eq. (S12). However, both the GBZ and the continuous part of the spectra is determined only by $\det(H - E\mathbb{1}) = 0$, which has 8 DOFs. The quantities $\langle h_0, h_0 \rangle$ and $\langle h_-, h_+ \rangle$ appear together as $\langle h_0, h_0 \rangle + 2\langle h_-, h_+ \rangle$ in the band structure and account for the lost DOF. By tuning this remaining DOF, the edge states can be moved around in the complex E plane while preserving the continuous part of the spectra. As such, any definitions of gaps that are based solely on the continuous part of the spectra cannot be used to predict the existence of symmetry-broken edge states.

B. GBZ Braiding

The definition of gap closing condition can be made more precise if we put additional constraints on the topology of the GBZ. One such condition for a two-band model is to require \mathcal{C}_{GBZ} to be a braid with two non-intersecting strands in the complex E plane with $\arg(z)$ as its parameter. Possible reasons for \mathcal{C}_{GBZ} not being a braid include three or more states with the same $\arg(z)$ or a disconnected GBZ with more than two components. SM Sec. VIII C gives some examples where the \mathcal{C}_{GBZ} is a braid [51, 52], and SM Sec. VIII D gives some examples where \mathcal{C}_{GBZ} is not a braid [59].

When \mathcal{C}_{GBZ} is a well-defined braid, the braid crossing number can be found by counting the number of branch points contained in the GBZ [68]. More precisely:

$$\# \text{ crossing number} = \frac{1}{2} \frac{1}{2\pi i} \int_{\mathcal{C}_{\text{GBZ}}} dz \frac{d}{dz} \ln \Delta = \# \text{ enclosed } z\text{-branch points} - \# \text{ poles} \quad (\text{S42})$$

where Δ is defined in Eq. (S18) with z branch points as its zeros, the $\#$ enclosed branch points is the count of z branch points in the same region divided by \mathcal{C}_{GBZ} as $z = 0$, and the $\#$ poles are the order of the $z = 0$ pole of Δ . Since a branch point induces a degenerate zero on the Riemann surface, it must have an even winding number with respect to any loop derived from the Riemann surface, and therefore cannot have a $|z|$ value sandwiched between the

two GBZ states at any $\arg(z)$. This allows collapsing \mathcal{C}_{GBZ} onto a single loop without passing through any branch points, and the results from Ref. [68] apply.

For the \mathcal{C}_{GBZ} braid, the gap closing condition can be defined as when the two strands intersect at the same complex E at a certain $\arg(z)$. This is accompanied by z branch points moving through the GBZ and a change in the topology of the braid. Within the restrictions of \mathcal{C}_{GBZ} being a braid, this allows dividing the model into several classes. A crossing number of 0 corresponds to an unlink, a crossing number of ± 1 corresponds to an unknot, and a crossing number of ± 2 corresponds to a Hopf link. The knot topology also determines the number of \mathcal{C}_{GBZ} components on the Riemann surface: an unlink or a Hopf link indicates two connected components of \mathcal{C}_{GBZ} , while an unknot indicates a single connected component of \mathcal{C}_{GBZ} . We note that both an unknot and a Hopf link lead to an OBC spectrum with a single connected component, while an unlink may correspond to an OBC spectrum with either one or two components [51, 52]. Having one or two OBC spectrum components is the same condition as closed or open line-gap of the OBC on the E plane, respectively.

For generic models given by Eq. (1), Δ has a pole of order 2 at $z = 0$. As such, if \mathcal{C}_{GBZ} forms braids, the knot topology can be inferred from the number of z branch points enclosed. In the unlink phase, \mathcal{C}_{GBZ} encloses 2 of the 4 z -plane branch points on the z -plane. Similarly, in the unknot phase, 1 or 3 branch points are enclosed, and in the Hopf link phase, 0 or 4 branch points are enclosed. Despite that each $\arg(z)$ has two GBZ states, the enclosure is well-defined since there are no branch points located between the two branches of the GBZ.

C. Edge states for different \mathcal{C}_{GBZ} eigenvalue braid topologies

Here we list some example models with different \mathcal{C}_{GBZ} braidings. In Table. II and Fig. S6 the \mathcal{C}_{GBZ} is an unlink; in Table. III and Fig. S7 the \mathcal{C}_{GBZ} is an unknot braid; in Table. IV and Fig. S8 the \mathcal{C}_{GBZ} is a Hopf link braid. For each class of braiding topology, the model can possess 0, 1 or 2 edge states.

Model	h_-		h_0		h_+	
$H_{\text{unlink0edge}}$	$1 + 0.5i$	1	1.5	-0.5	i	0
	0.1	0.3	0.2	0	1	$0.2 - 0.5i$
$H_{\text{unlink1edge}}$	$1 + 0.5i$	1	0.5	-0.5	i	0
	0.1	0.3	0.2	0	1	0.2
$H_{\text{unlink2edge}}$	$1 + 0.5i$	1	0.5	-0.5	i	0
	0.1	$0.3 + 0.5i$	0.2	0	1	0.2

TABLE II. Example model parameters for when \mathcal{C}_{GBZ} is an unlink braid.

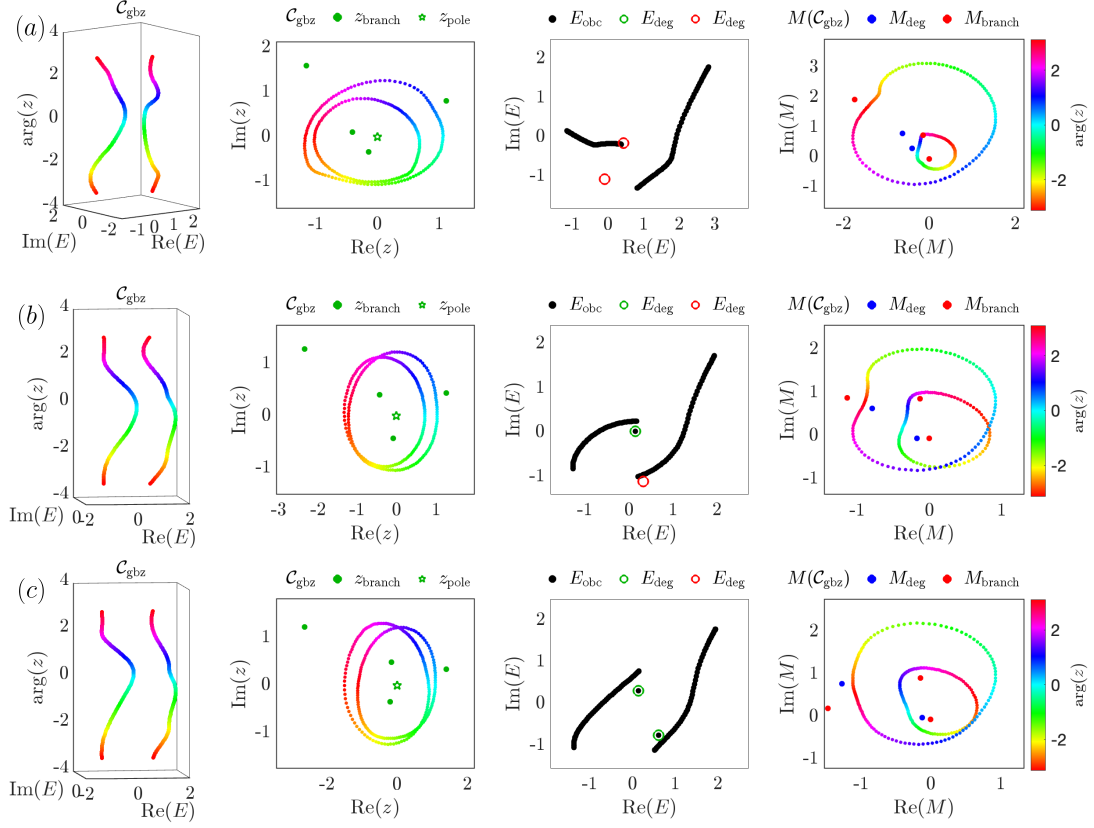
\mathcal{C}_{gbz} is an unlink

FIG. S6. The first subplot is \mathcal{C}_{GBZ} in $\{\text{Re}(E), \text{Im}(E), \arg(z)\}$ space colored by $\arg(z)$ of \mathcal{C}_{GBZ} . The second subplot is \mathcal{C}_{GBZ} on the z -plane colored by $\arg(z)$ of \mathcal{C}_{GBZ} with z_{branch} and z_{pole} as green dots and stars respectively. The third subplot is the OBC spectrum for $N = 60$ and E_{deg} plotted as a green circle if it corresponds to an edge state and a red circle if it does not. The fourth subplot is $M(\mathcal{C}_{\text{GBZ}})$ colored by $\arg(z)$ of \mathcal{C}_{GBZ} with M_{deg} and M_{branch} in blue and red dots respectively. (a)-(c) are for $H_{\text{unlink0edge}}, H_{\text{unlink1edge}}, H_{\text{unlink2edge}}$ respectively in Table. II

Model	h_-		h_0		h_+	
$H_{\text{unknot0edge}}$	-0.6	0.4	0.6	0.9	-2	-0.4
	12	-1.7	1.2	-2	1	-1.8
$H_{\text{unknot1edge}}$	-0.6	0.4	0.6	0.9	-2	-0.4
	2	-1.7	1.2	-2	1	-1.8
$H_{\text{unknot2edge}}$	-0.6	0.4	0.6	0.9	-2	-0.4
	1	-1.7	1.2	-2	1	-1.8

TABLE III. Example model parameters for when \mathcal{C}_{GBZ} is an unknot braid.

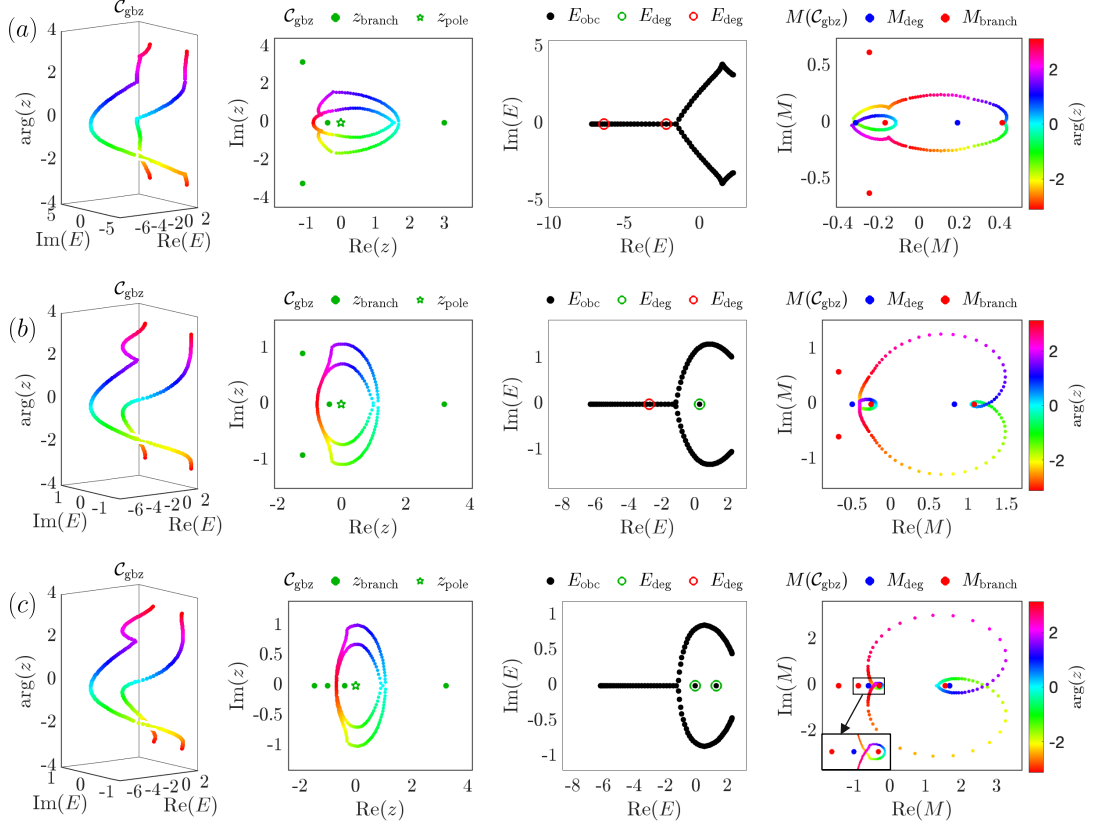
\mathcal{C}_{gbz} is an unknot

FIG. S7. The first subplot is \mathcal{C}_{GBZ} in $\{\text{Re}(E), \text{Im}(E), \arg(z)\}$ space colored by $\arg(z)$ of \mathcal{C}_{GBZ} . The second subplot is \mathcal{C}_{GBZ} on the z -plane colored by $\arg(z)$ of \mathcal{C}_{GBZ} with z_{branch} and z_{pole} as green dots and stars respectively. The third subplot is the OBC spectrum for $N = 60$ and E_{deg} plotted as a green circle if it corresponds to an edge state and a red circle if it does not. The fourth subplot is $M(\mathcal{C}_{\text{GBZ}})$ colored by $\arg(z)$ of \mathcal{C}_{GBZ} with M_{deg} and M_{branch} in blue and red dots respectively. (a)-(c) are for $H_{\text{unknot0edge}}, H_{\text{unknot1edge}}, H_{\text{unknot2edge}}$ respectively in Table. III.

Model	h_-	h_0	h_+
$H_{\text{hopf0edge}}$	$\begin{bmatrix} -1 & 0.2 \\ 0.2 & -1 \end{bmatrix}$	$\begin{bmatrix} 1.7 & 0.3i \\ 0 & -1.7 \end{bmatrix}$	$\begin{bmatrix} 0 & -12 \\ 1 & 0 \end{bmatrix}$
$H_{\text{hopf1edge}}$	$\begin{bmatrix} -1 & 0.2 \\ 0.2 & -1 \end{bmatrix}$	$\begin{bmatrix} 1.7 - 0.1i & 0.3i \\ 0 & -1.7 \end{bmatrix}$	$\begin{bmatrix} -0.16 + 0.3i & -12 \\ 0.1 & 0 \end{bmatrix}$
$H_{\text{hopf2edge}}$	$\begin{bmatrix} -1 & 0.2 \\ 0.2 & -1 \end{bmatrix}$	$\begin{bmatrix} 1.7 & 0.3i \\ 0 & -1.7 \end{bmatrix}$	$\begin{bmatrix} 0 & -12 \\ 0.1 & 0 \end{bmatrix}$

TABLE IV. Example model parameters for when \mathcal{C}_{GBZ} is a hopf link braid.

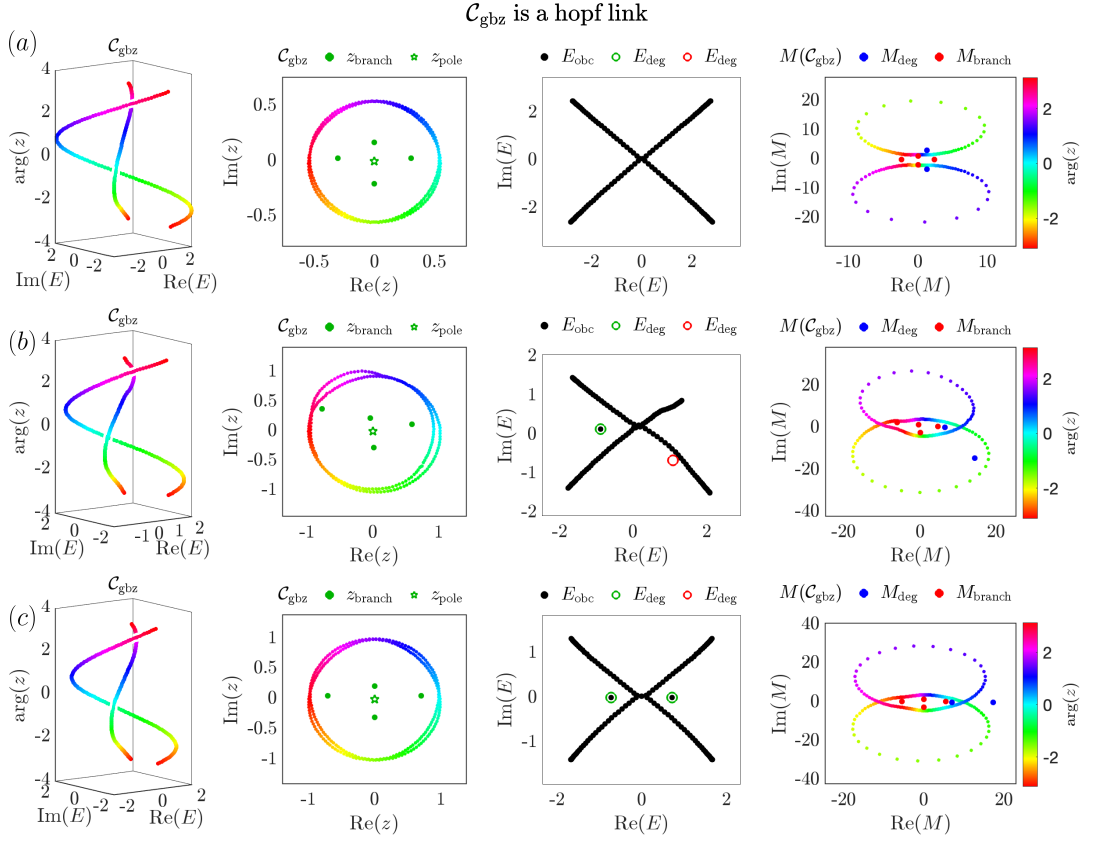


FIG. S8. The first subplot is \mathcal{C}_{GBZ} in $\{\text{Re}(E), \text{Im}(E), \arg(z)\}$ space colored by $\arg(z)$ of \mathcal{C}_{GBZ} . The second subplot is \mathcal{C}_{GBZ} on the z -plane colored by $\arg(z)$ of \mathcal{C}_{GBZ} with z_{branch} and z_{pole} as green dots and stars respectively. The third subplot is the OBC spectrum for $N = 60$ and E_{deg} plotted as a green circle if it corresponds to an edge state and a red circle if it does not. The fourth subplot is $M(\mathcal{C}_{\text{GBZ}})$ colored by $\arg(z)$ of \mathcal{C}_{GBZ} with M_{deg} and M_{branch} in blue and red dots respectively. (a)-(c) are for $H_{\text{hopf0edge}}, H_{\text{hopf1edge}}, H_{\text{hopf2edge}}$ respectively in Table. IV.

In Table. V and Fig. S9 we give an example of a non-Hermitian model where Eq. (9) does not apply but Eq. (10) applies. While the braiding topology of \mathcal{C}_{GBZ} is an unlink similar to Hermitian models, the $M(\mathcal{C}_{\text{GBZ}})$ loops has intersections, invalidating the combinatorial argument in SM Sec. VII.

Model	h_-	h_0	h_+
H_{counter}	-1.0 -6.5i	0 3.5i	0.5 0.7i
	0.3i -1.0	1.0i 0	0.7i 0.7

TABLE V. Example model parameters for H_{counter} .

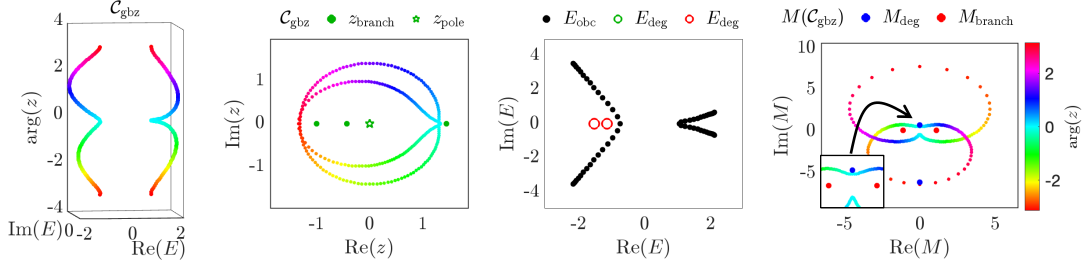


FIG. S9. The first subplot is \mathcal{C}_{GBZ} in $\{\text{Re}(E), \text{Im}(E), \arg(z)\}$ space colored by $\arg(z)$ of \mathcal{C}_{GBZ} . The second subplot is \mathcal{C}_{GBZ} on the z -plane colored by $\arg(z)$ of \mathcal{C}_{GBZ} with z_{branch} and z_{pole} as green dots and stars respectively. The third subplot is the OBC spectrum for $N = 60$ and E_{deg} plotted as a green circle if it corresponds to an edge state and a red circle if it does not. The fourth subplot is $M(\mathcal{C}_{\text{GBZ}})$ colored by $\arg(z)$ of \mathcal{C}_{GBZ} with M_{deg} and M_{branch} in blue and red dots respectively. The model is H_{counter} from Table. V

D. Examples when the GBZ is not a braid

There are also cases where \mathcal{C}_{GBZ} does not define a braid at all. One possible reason is the appearance of more than three states for a single $\arg(z)$, as listed in Table. VI and Fig. S10. While it is possible to choose parameters other than $\arg(z)$ for the first model that follows the strand and define a braid, the disconnected part in the second model cannot be fixed this way. However, the general edge state invariant in Eq. (10) holds in these cases if the integral goes over each piece of \mathcal{C}_{GBZ} .

Model	h_-		h_0		h_+	
H_{notbraid}	$0.914 - 0.3i$	$-0.388 + 0.6i$	$0.45 + 0.128i$	$-1.208 - 0.79i$	$-1.45 + 0.15i$	$0.83 + 0.6i$
	$-0.562 + 0.224i$	$0.426 - 0.324i$	$-0.192 - 0.612i$	$0.056 - 0.764i$	$0.428 + 0.824i$	$-0.884 + 0.39i$
$H_{\text{disconnected}}$	$0.97 - 0.34i$	$-0.186 + 0.706i$	$-0.02 - 0.216i$	$-1.07 - 1.176i$	$-1.15 - 0.24i$	$0.866 - 0.43i$
	$-0.362 + 0.16i$	$0.404 - 0.15i$	$0 - 0.74i$	$0.25 - 0.73i$	$0.206 + 1.022i$	$-0.956 + 0.252i$

TABLE VI. Example model parameters for when \mathcal{C}_{GBZ} is not braid.

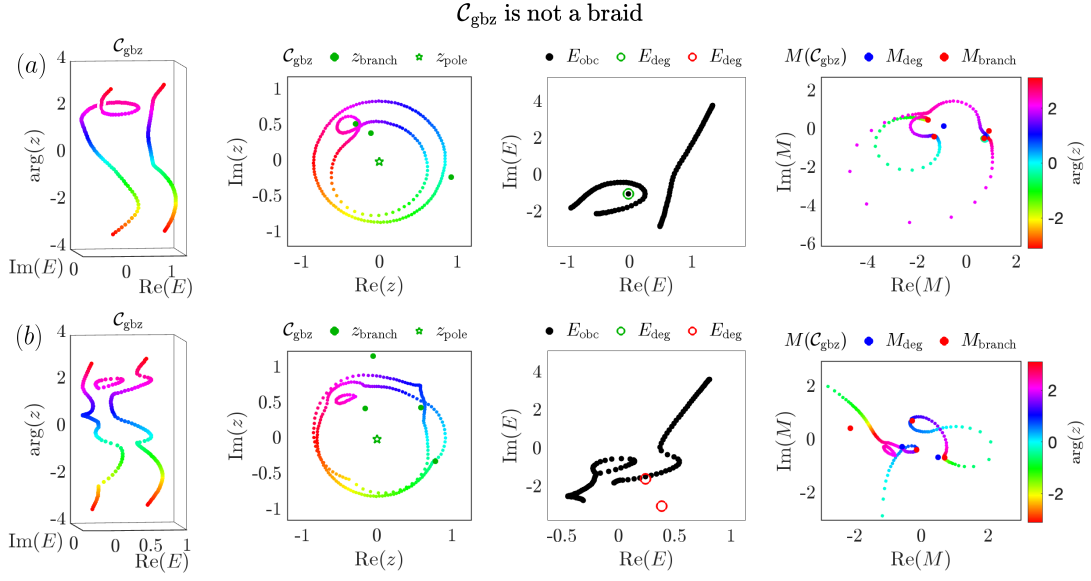


FIG. S10. The first subplot is \mathcal{C}_{GBZ} in $\{\text{Re}(E), \text{Im}(E), \text{arg}(z)\}$ space colored by $\text{arg}(z)$ of \mathcal{C}_{GBZ} . The second subplot is \mathcal{C}_{GBZ} on the z -plane colored by $\text{arg}(z)$ of \mathcal{C}_{GBZ} with z_{branch} and z_{pole} as green dots and stars respectively. The third subplot is the OBC spectrum for $N = 60$ and E_{deg} plotted as a green circle if it corresponds to an edge state and a red circle if it does not. The fourth subplot is $M(\mathcal{C}_{\text{GBZ}})$ colored by $\text{arg}(z)$ of \mathcal{C}_{GBZ} with M_{deg} and M_{branch} in blue and red dots respectively. (a) and (b) are for H_{notbraid} and $H_{\text{disconnected}}$ respectively in Table. VI.

Another possible reason for non-braids is when z branch points are on the GBZ, creating intersections of the strands. Here we consider an SSH model with on site gain and loss [98]:

Model	h_-	h_0	h_+
$H_{\text{onsitessh}}$	$\begin{vmatrix} 0 & t_2 \\ 0 & 0 \end{vmatrix}$	$\begin{vmatrix} i\gamma & t_1 \\ t_1 & -i\gamma \end{vmatrix}$	$\begin{vmatrix} 0 & 0 \\ t_2 & 0 \end{vmatrix}$

TABLE VII. Example model parameters for when \mathcal{C}_{GBZ} coalesces.

For $t_1 = 1.5, 1, 0.3$ where $\gamma = 1, t_2 = 1$, there are two z -plane branch points on \mathcal{C}_{GBZ} , and the two bands coalesce at these points. Despite this, there is an edge state transition for these parameter changes. This is reminiscent of Hermitian critical gapless edge states [80]. The general edge state invariant also apply to this case. In Fig. S11 we see that the M_{deg} moves to different regions encircled by $M(\mathcal{C}_{\text{GBZ}})$ as the edge state transitions occur.

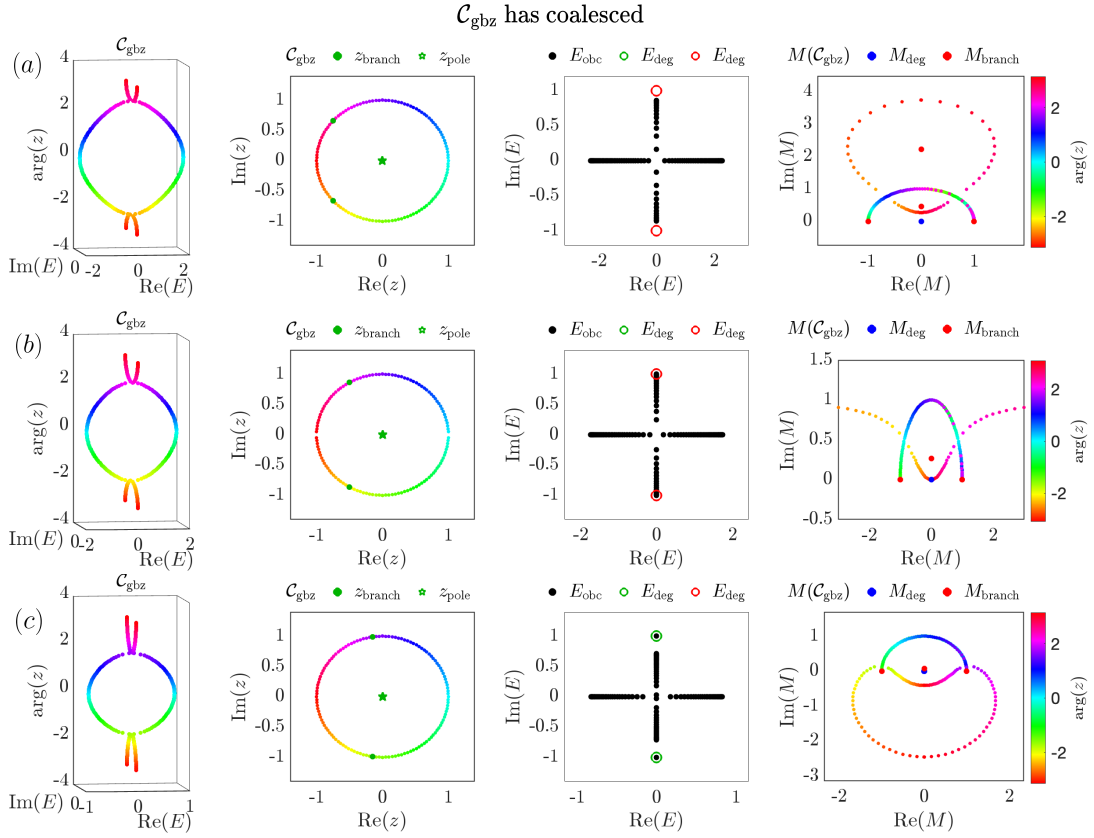


FIG. S11. The first subplot is \mathcal{C}_{GBZ} in $\{\text{Re}(E), \text{Im}(E), \arg(z)\}$ space colored by $\arg(z)$ of \mathcal{C}_{GBZ} . The second subplot is \mathcal{C}_{GBZ} on the z -plane colored by $\arg(z)$ of \mathcal{C}_{GBZ} with z_{branch} and z_{pole} as green dots and stars respectively. The third subplot is the OBC spectrum for $N = 60$ and E_{deg} plotted as a green circle if it corresponds to an edge state and a red circle if it does not. The fourth subplot is $M(\mathcal{C}_{\text{GBZ}})$ colored by $\arg(z)$ of \mathcal{C}_{GBZ} with M_{deg} and M_{branch} in blue and red dots respectively. (a)-(c) is for $H_{\text{onsitessh}}$ in Table VI where $\gamma = 1, t_2 = 1$ and $t_1 = 1.5, 1, 0.3$ respectively.

IX. VISUALIZATION OF THE M -INVARIANT AS AN INDEX TRACKER

In the main text, we stated that the edge-state invariants are index trackers used to determine whether M_{deg} corresponds to the edge-state condition. We now discuss two different visualizations of this argument. In this section, we will use the following model:

$$H = (1 - \alpha)H_{\text{nh2}} + \alpha H_{\text{ssh}} \quad (\text{S43})$$

where H_{nh2} is given by:

Model	h_-	h_0	h_+
H_{nh2}	$0.51 + 0.40i$ $-0.44 + 0.38i$	$-0.18 + 0.32i$ $-0.33 + 0.70i$	$0.74 - 0.13i$ $-0.43 - 0.08i$
	$-0.86 + 0.40i$ $-0.86 - 0.03i$	$-0.44 - 0.84i$ $0.21 - 0.74i$	$-0.79 - 0.84i$ $0.01 + 0.60i$

A. Edge state transition on $M(E)$ sheets and winding on M -plane

While the collection of (M, E) points does not form a Riemann surface due to the degeneracy, we can still obtain four M values at each E and thus define four $M(E)$ sheets. The bulk eigenvector degeneracies occur when the $M(E)$ sheets touch and show up as minima in $\log(|M_i - M_j|)$, where $i \neq j$ and the i, j labels are derived from the z solution orderings. The z -plane branch points will also show up as minima, but these are expected to be less prominent than the bulk eigenvector degeneracies (due to the square-root behavior near the branch points). This gives an alternative

numerical method for locating M_{deg} , in contrast to the analytical methods described in SM Sec. III. In the first subpanel of Fig. S12 to S14, we plot the minimum $\log(|M_i - M_j|)$ among all pairs of M_i and M_j . The analytical edge state condition is applied and we plot E_{deg} as a green circle if it is an edge state and red if it is not. The z -plane branch points are analytically solved and circled in blue. In the second subpanel of Fig. S12 to S14, we plot E_{obc} so that the edge states can be clearly seen. In the third subpanel of Fig. S12 to S14, we plot the $z(E)$ projection of Eq. (4). The OBC for $N = 60$ is plotted in black. At E_{deg} there are two of the four z values that correspond to M_{deg} . In this third subpanel, we plot these two z values as a green dot if it corresponds to an edge state and red if it does not. In this panel, the sheets are $z_1(E)$ to $z_4(E)$ from top to bottom respectively. This allows us to visually count the i, j indices from z_i, z_j in the green or red dots that correspond to the $M_i = M_j$ condition for M_{deg} . In the fourth subpanel of Fig. S12 to S14, we plot the image of \mathcal{C}_{GBZ} on the M -plane colored by the $\arg(z)$ it corresponded to. We also plot M_{deg} and which M_{branch} which allows us to calculate the edge-state invariant.

From Fig. S12 to S14 the number of edge states go from 2 to 1 to 0. We see that the E_{deg} point must move past the E_{GBZ} line as this is where the corresponding M_i indices change. We also see how this E_{deg} point moving past the E_{GBZ} line is related to the M_{deg} point moving in or out of the $M(\mathcal{C}_{\text{GBZ}})$ loops. The distance of a E_{deg} point from E_{GBZ} (even when it is not an edge state) provides some notion of how far M_{deg} is from the boundaries of the $M(\mathcal{C}_{\text{GBZ}})$ loops, which is an indication of the robustness of forming or removing an edge state.

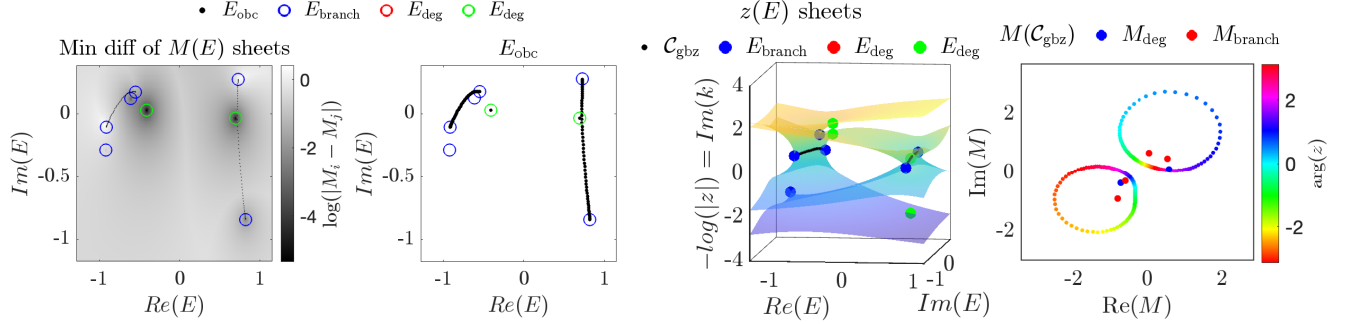


FIG. S12. Two edge states, $\alpha = 0.5, t_1 = 1, t_2 = 0.7$ for Eq. (S43). Here, the two E_{deg} points correspond to $M_1 = M_2, M_3 = M_4$.

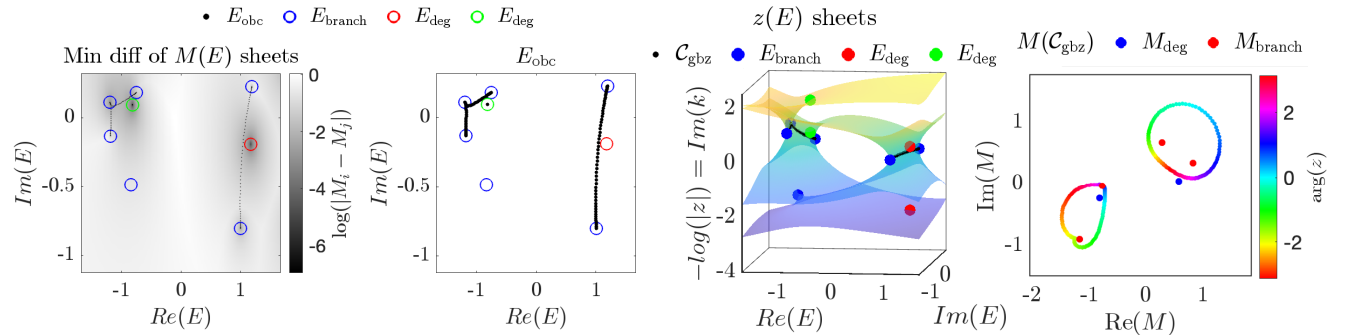


FIG. S13. One edge state, $\alpha = 0.5, t_1 = 2, t_2 = 0.9$ for Eq. (S43). Here, the two E_{deg} points correspond to $M_1 = M_2, M_2 = M_4$.

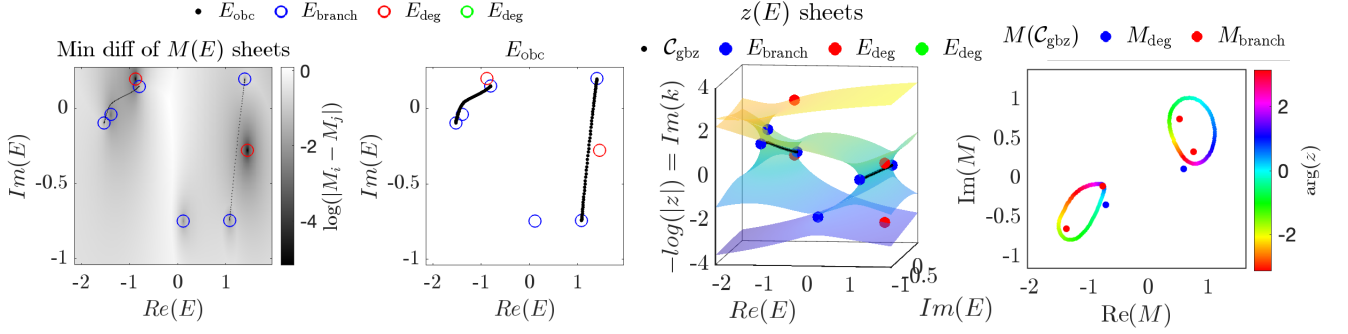


FIG. S14. No edge states, $\alpha = 0.5, t_1 = 2.5, t_2 = 0.7$ for Eq. (S43). Here, the two E_{deg} points correspond to $M_1 = M_3, M_2 = M_4$.

B. Auxiliary GBZ on the M -Riemann sphere

Another way to visualize Eq. (9) and Eq. (10) as an index tracker for M is to represent the allowed M_i regions on the M -Riemann sphere. The different M_i regions containing M_{deg} indicate the indices of the $M_i = M_j$ condition for M_{deg} . Note that M_1 to M_4 are different from the $z(M)$ or $E(M)$ sheets and instead refer to the $M(E)$ sheets. The coverage can be determined by sampling the E values, numerically solving for the four $z_i(E)$ solutions, then mapping this to $M_i(E)$ using Eq. (5). The lines demarcating the different M_i regions are given by the image of the auxiliary GBZ [61] on the M -Riemann sphere. The auxiliary GBZ for Eq. (1) are the solutions to Eq. (4) where $|z_1| = |z_2|, |z_2| = |z_3|$ or $|z_3| = |z_4|$.

In Fig. S15 we use Eq. (S43) with $\alpha = 0.9$ and $t_1 = 0.5, t_2 = 1$ for the SSH parameters. This example model contains two edge states. We denote M_{12} branch, M_{23} branch, and M_{34} branch as the images of the auxiliary GBZ $|z_1| = |z_2|, |z_2| = |z_3|$ and $|z_3| = |z_4|$ on the M -Riemann sphere. We plot the M_{deg} points in black triangle and square markers. We color the M_1 to M_4 regions in red, yellow, blue and purple respectively. Some of the M_i regions cover parts of the M -Riemann sphere twice, and the colors are more saturated in such regions. We see in Fig. S15 that one of the M_{deg} points lies in a region where the M -Riemann sphere is covered by an M_1 and M_2 region and the other M_{deg} point lies in a region where the M -Riemann sphere is covered by an M_3 and M_4 region. Thus, both M_{deg} points satisfy the condition for an edge state.

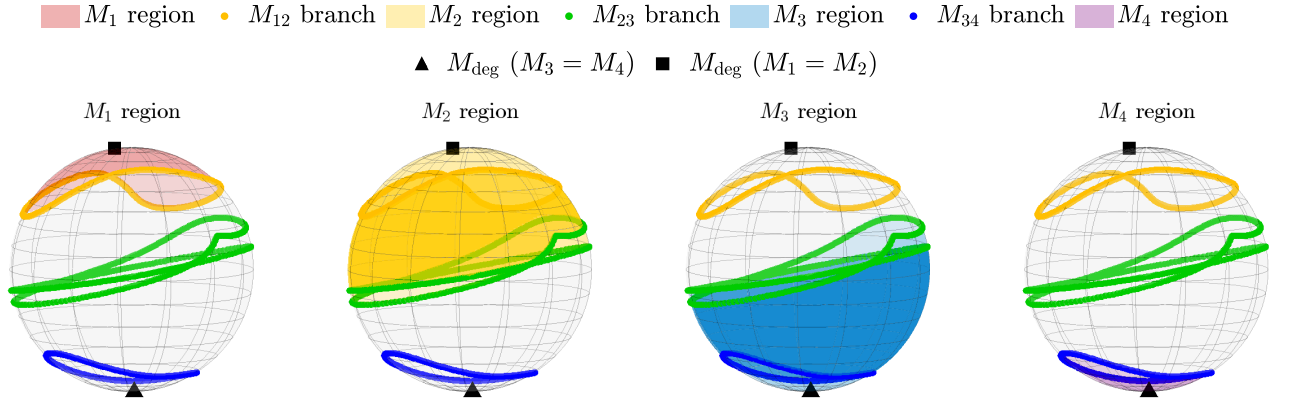


FIG. S15. The two M_{deg} points lie in the M_1, M_2 region and the M_3, M_4 regions, corresponding to two edge states. Here, we have $\alpha = 0.9, t_1 = 0.5, t_2 = 1$ for the model in Eq. (S43).

In Fig. S16 we use Eq. (S43) with $\alpha = 0.9$ and $t_1 = 1.5, t_2 = 1$ for the SSH parameters. This example model contains two edge states. By including the images of the auxiliary GBZ, we see that the M_{deg} points lie in a region where the M -Riemann sphere is covered by an M_1 and M_3 region as well as a M_2 and M_4 region respectively, which is the condition that does not lead to an edge state.

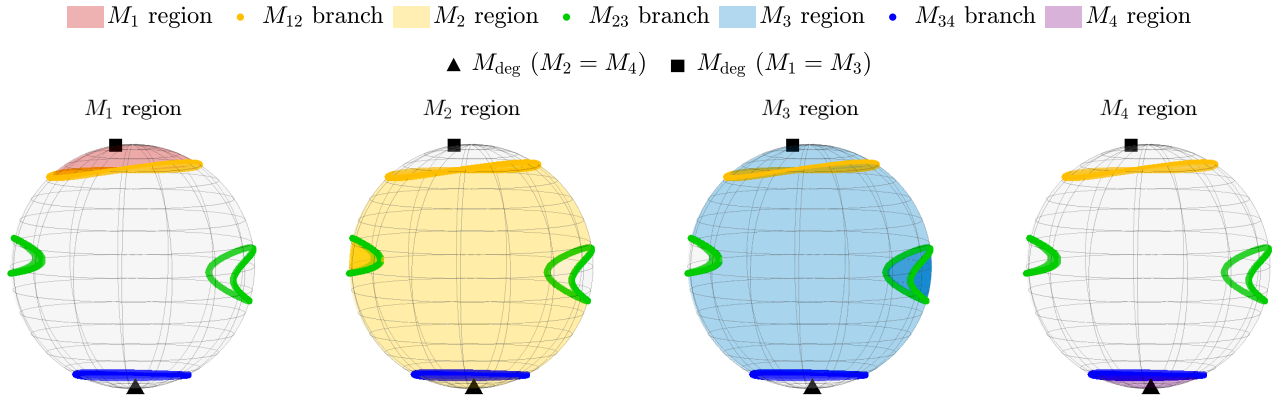


FIG. S16. The two M_{deg} points lie in the M_1, M_3 allowed region and the M_2, M_4 allowed regions, corresponding to no edge states. Here, we have $\alpha = 0.9, t_1 = 1.5, t_2 = 1$ for the model in Eq. (S43).